

Massive stars and the energy balance of the ISM.

I. The impact of an isolated $60 M_{\odot}$ star

Tim Freyer and Gerhard Hensler

Institut für Theoretische Physik und Astrophysik der Universität, D-24098 Kiel, Germany

freyer@astrophysik.uni-kiel.de, hensler@astrophysik.uni-kiel.de

and

Harold W. Yorke

Jet Propulsion Laboratory, MS 169-506, 4800 Oak Grove Drive, Pasadena, CA 91109, USA

Harold.Yorke@jpl.nasa.gov

ABSTRACT

We present results of numerical simulations carried out with a 2D radiation hydrodynamics code in order to study the impact of massive stars on their surrounding interstellar medium. This first paper deals with the evolution of the circumstellar gas around an isolated $60 M_{\odot}$ star. The interaction of the photoionized H II region with the stellar wind bubble forms a variety of interesting structures like shells, clouds, fingers, and spokes. These results demonstrate that complex structures found in H II regions are not necessarily relics from the time before the gas became ionized but may result from dynamical processes during the course of the H II region evolution. We have also analyzed the transfer and deposit of the stellar wind and radiation energy into the circumstellar medium until the star explodes as a supernova. Although the total mechanical wind energy supplied by the star is negligible compared to the accumulated energy of the Lyman continuum photons, the kinetic energy imparted to the circumstellar gas over the star's lifetime is 4 times higher than for a comparable windless simulation. Furthermore, the thermal energy of warm photoionized gas is lower by some 55 %. Our results document the necessity to consider both ionizing radiation and stellar winds for an appropriate description of the interaction of OB stars with their circumstellar environment.

Subject headings: galaxies: evolution—H II regions—hydrodynamics—instabilities—ISM: bubbles—ISM: structure

1. Introduction

Massive stars play an important role in the evolutionary history of galaxies. They are the primary source of metals and dominate the turbulent energy input into the interstellar medium (ISM) by stellar winds, radiation, and supernova explosions. The radiation field of a massive star first dissociates the ambient molecular gas and forms a so-called photodissociation region of neutral hydrogen. Subsequently, the Lyman continuum photons of the star ionize the H I gas and produce an H II region that expands into the neutral ambient medium. A fast stellar wind creates shocks that form a so-called stellar wind bubble (SWB) filled with hot plasma, which expands into the H II region. Finally, the star explodes as a supernova of type II (SN II), creating a supernova remnant (SNR) that sweeps up the ambient medium. The SWBs and SNRs of neighboring stars can overlap and form a superbubble with a diameter of order 1 kpc.

This paper pursues two major goals. First, we want to examine the combined influence of wind and ionizing radiation on the dynamical evolution of circumstellar matter around massive stars, i.e. we are interested in the interaction processes between the photoionized H II region and the SWB that evolves into the ionized gas. The second goal is to improve our knowledge of the energy transfer efficiency between massive stars and the ISM: How and to what fraction is the energy of stellar radiation and the stellar wind converted into kinetic, thermal, and ionization energy of the ISM? How does the formation of the SWB influence the transfer of stellar radiation? To what extent does all this depend on the evolutionary state of the star?

To investigate these effects we perform numerical 2D radiation hydrodynamic simulations of the interaction between an isolated massive star and its surrounding ISM via stellar hydrogen-ionizing photons and a stellar wind. We calculate the hydrodynamical evolution of the circumstellar gas coupled with radiation transfer, time-dependent ionization of hydrogen, and a realistic description of cooling. The stellar mass-loss rate, the terminal velocity of the wind, the effective temperature, and the luminosity of the star are specified as time-dependent boundary conditions. We examine the evolution of the circumstellar material starting from the main sequence (MS) phase of the star until it explodes as a supernova. We do not consider the SNR formation. In this paper we present results of these calculations for a star with an initial mass of $60 M_{\odot}$, extending the work of García-Segura, Mac Low, & Langer (1996a, hereafter GML1) to a more precise analysis of the energetic aspect during the whole evolution of the star.

The remainder of this paper is structured as follows: In section 2 we briefly review theoretical and observational studies of H II regions and SWBs around massive stars for later comparison. Our numerical procedure as well as the initial conditions and time-dependent

boundary conditions are described in section 3. In section 4 we present the numerical results of our calculations and discuss them in the context of previous analytical approaches, other numerical investigations, and observations. Finally, in section 5 we summarize our main results and draw some conclusions from the work presented in this paper.

2. Theoretical concepts and observational constraints

2.1. H II regions

H II regions are observed in various sizes and shapes. Depending on their geometrical extent, they are labeled as ultracompact, compact, extended, or giant. The ultracompact (linear size $\lesssim 0.1$ pc) and partly also the compact (0.1–0.3 pc) H II regions are still deeply embedded in their birthplaces, mature molecular clouds, and due to dust obscuration generally are only observable in the IR and radio wavelengths. On the other hand, extended H II regions with sizes up to several parsecs and giant H II regions which are composed of individual H II regions and have sizes of a few 100 pc are often easily discernible in the optical by their bright Balmer and forbidden metal lines. Large holes and shells make it obvious that the giant H II regions are not only powered by stellar radiation but also by stellar winds and supernova explosions in the underlying OB star cluster (see e.g. Yang et al. 1996).

Within the framework of the simplest theoretical approach an O star suddenly “turns on” in a constant density, motionless medium and begins to ionize its surroundings. The reaction of the medium to the stellar photons is well-known and has been described in detail in standard textbooks (see e.g. Spitzer 1978). For comparison purposes with our numerical results we are particularly interested in the time evolution of the location r_i of the ionization front:

$$r_i = \left(\frac{7}{4} c_{\text{s,II}} r_0^{3/4} \tau + r_0^{7/4} \right)^{4/7} \quad (1)$$

$$r_0 = \left(\frac{3L_{\text{LyC}}}{4\pi n_0^2 \beta^{(2)}(T)} \right)^{1/3}, \quad (2)$$

where $c_{\text{s,II}}$ is the isothermal sound speed of the ionized gas, r_0 the initial Strömgren radius, L_{LyC} the photon luminosity in the Lyman continuum, n_0 the hydrogen number density in the neutral ambient medium, $\beta^{(2)}(T)$ the coefficient for recombinations of hydrogen into levels 2 and higher, and τ the age of the star. According to Lasker (1967) the kinetic energy of the expanding swept-up shell is

$$E_k = \frac{4}{3} \pi n_0 m_H c_{\text{s,II}}^2 r_0^{3/2} \left[\left(\frac{7}{4} c_{\text{s,II}} r_0^{3/4} \tau + r_0^{7/4} \right)^{6/7} - r_0^{3/2} \right], \quad (3)$$

where m_{H} is the mass of a hydrogen atom. Because this swept-up shell can be expected to remain cool and neutral due to strong radiative cooling, we can also estimate the ionization energy stored in the H II region:

$$E_{\text{i}} = \frac{4}{3} \pi n_0 \left(\frac{7}{4} c_{s,\text{II}} r_0^{5/2} \tau + r_0^{7/2} \right)^{6/7} \chi_0 . \quad (4)$$

Here we have used equation (2) for the time-dependent radius of the ionization front and χ_0 is the ionization potential of hydrogen in the ground state.

The same ansatz can then be used to estimate the thermal energy of warm gas in the H II region:

$$E_{\text{t}} = 4 \pi n_0 \left(\frac{7}{4} c_{s,\text{II}} r_0^{5/2} \tau + r_0^{7/2} \right)^{6/7} k_{\text{B}} T_{\text{II}} , \quad (5)$$

where we will insert $T_{\text{II}} = 8000 \text{ K}$ as an appropriate approximation to the temperature in the H II region. k_{B} is the Boltzmann constant.

2.2. Theory of stellar wind bubbles

First considerations about the inner structure of SWBs go back to Pikel'ner (1968), Avedisova (1972), Dyson & de Vries (1972), and Dyson (1973), but the work of Castor, McCray, & Weaver (1975) and Weaver et al. (1977) set a milestone in the approach of understanding SWBs. They presented a fairly complete picture of the structure and evolution of SWBs together with a set of equations that describes the evolution under the simplifying assumptions of a point source of a constant and spherically symmetric strong wind that interacts with a homogeneous ambient ISM. The global structure that arises from such a wind-ISM interaction is depicted in Figure 1 together with the expanding H II region into which the SWB evolves. It consists of a free-flowing supersonic wind that is heated to about $10^6 - 10^8 \text{ K}$ when it passes the inner reverse shock at r_{s1} . The pressure of this hot rarefied gas that normally fills most of the volume of the SWB is typically much higher than the pressure in the photoionized ambient medium. As a consequence, the hot gas bubble expands into the H II region producing a forward shock at r_{s2} that sweeps up the gas from the H II region in a shell which is separated from the hot bubble interior by a contact discontinuity at r_c .

Three phases in the evolution of such a bubble can be distinguished: The first is the adiabatic phase that lasts until the shock speed v_{s2} drops below 200 km s^{-1} (Falle 1975), typically a few 10 to a few 1000 yr, depending on the mechanical luminosity of the wind and on the ambient density. The bubble is expanding so fast that radiative cooling does not play a significant role for the dynamical behavior. The second stage of evolution is characterized

by strong cooling in the shell of swept-up material (between r_c and r_{s2}), allowing it to be compressed into a geometrically thin ($r_c(t) = r_{s2}(t)$, where t denotes time), dense shell, whereas for the hot bubble (between r_{s1} and r_c) cooling is still negligible. This phase lasts much longer than the first, so-called adiabatic phase. Thermal conduction from the hot bubble interior to the collapsed shell may become important and may modify the structure of the bubble in this stage. Weaver et al. (1977) assume that an equilibrium between the conductive energy flux and the mechanical energy flux due to evaporation of shell mass in the reverse direction is established. Under the assumptions that in the hot bubble between r_{s1} and $r_c = r_{s2}$ the pressure is everywhere the same and that the thermal energy contained within this region is much higher than the kinetic energy, Weaver et al. (1977) derived the following equations for the temporal dependence of the radius $r_{s2}(t)$ and the pressure in the hot bubble $P_b(t)$ in this stage:

$$r_{s2}(t) = r_c(t) = \left(\frac{125}{154\pi} \right)^{1/5} L_w^{1/5} \rho_0^{-1/5} t^{3/5}, \quad (6)$$

$$P_b(t) = \frac{7}{(3850\pi)^{2/5}} L_w^{2/5} \rho_0^{3/5} t^{-4/5}. \quad (7)$$

$\rho_0 = n_0 m_H$ is the density of the ambient medium and $L_w = \frac{1}{2} \dot{M}_w v_w^2$ the stellar wind luminosity, with \dot{M}_w and v_w being the mass-loss rate and the terminal velocity of the star.

It is also possible to obtain an analytical result for the energy that is deposited in the ISM by SWBs. We neglect the first (fully adiabatic) stage of bubble evolution because it is very short. Cooling in the hot bubble strongly depends on the efficiency of heat conduction, or, how efficiently heat conduction is suppressed by magnetic fields. We will assume for the analytical theory that there is no heat conduction and thus cooling in the hot bubble is unimportant during the lifetime of the star. The hot bubble acts like a piston on the ambient medium and analogous to the case of an H II region it can be shown that the PdV work is equally distributed on kinetic energy of shell motion and thermal energy in the shell (which gets immediately lost due to cooling). If we furthermore assume that the kinetic energy of the stellar wind is completely transformed into thermal energy at the reverse shock (the strong-jump conditions give 15/16, but clumpiness of the stellar wind, which we completely neglect, might reduce this value), we get for the kinetic energy:

$$E_k = \frac{1}{2} \int_0^{V_{s2}(\tau)} P_b dV_{s2}. \quad (8)$$

V_{s2} is the volume inside r_{s2} . Using equation (6) for r_{s2} and equation (7) for the pressure in the hot bubble yields

$$E_k = \frac{3}{11} L_w \tau. \quad (9)$$

The thermal energy of the hot gas is thus

$$E_t = L_w \tau - \int_0^{V_{s2}(\tau)} P_b dV_{s2} = \frac{5}{11} L_w \tau . \quad (10)$$

Besides heat conduction and cooling in the hot bubble we have also neglected the fact that part of the thermal energy might be used for collisional ionization of gas. Thus, the results for E_k and E_t are upper limits.

Though the analytical and semi-analytical solutions for the evolution of SWBs have been improved in recent years (Koo & McKee 1992a,b; García-Segura & Mac Low 1995; Pittard, Dyson, & Hartquist 2001a; Pittard, Hartquist, & Dyson 2001b) a variety of physical effects remains to be included in order to achieve a better agreement of models and observations. For example, the discrepancy between models and observations with regard to the evolution of the hot phase in bubbles has recently been reviewed by Mac Low (2000). See also Chu (2000). It has become evident that the stellar parameters such as the mass-loss rate, the terminal velocity, the effective temperature and the luminosity of the star which drive the evolution of the circumstellar matter vary strongly over time. Because most previous studies dealt with either the evolution of H II regions or of SWBs, little is known about the interaction of these two structures.

2.3. Observations of stellar wind bubbles

Hot gas ($10^6 - 10^8$ K) is expected to be a crucial indicator for the existence of SWBs. However, there have been only two successful X-ray observations of SWBs so far: NGC 6888 (Bochkarev 1988; Wrigge, Wendker, & Wisotzki 1994) and S308 (Wrigge 1999). Both are actually Wolf-Rayet (WR) bubbles (i.e. the wind-driving star has already entered its WR stage). The fact that no MS bubble has yet been observed in X-rays may be due to their physical properties; they are expected to be large, diffuse, and consequently dim (compared with WR bubbles). There may also be a problem with the theoretical models. More sensitive X-ray telescopes of the next generation should be able to illuminate this problem.

The shells of MS bubbles are also difficult to observe in the optical because they are large and dim (McKee, Van Buren, & Lazareff 1984). Nevertheless, shells around MS stars as well as shells around evolved massive stars, which — based on their radius, expansion velocities, and shell mass — are considered to originate from the MS phase of these stars, have been observed in the optical (Lozinskaya 1982; Oey & Massey 1994; Marston 1997), in the IR (Marston 1996), and in the H I 21 cm line (Cappa et al. 1996; Cappa & Benaglia 1998; Benaglia & Cappa 1999).

The MS shells are typical results of the interaction of massive stars with their surrounding ISM over a time period of a few Myr. There are also young objects which have influenced their interstellar environment so strongly that they can already be identified as star-gas interactions. One example that should certainly be mentioned here is the so-called Becklin-Neugebauer-Kleinman-Low (BN-KL) nebula in the Orion molecular cloud 1 (OMC1) behind the Orion nebula. It shows a spectacular, finger-like outflow of molecular hydrogen (Taylor et al. 1984; Allen & Burton 1993; McCaughrean & Mac Low 1997; Salas et al. 1999). Due to extremely high visual extinction ($A_V \approx 20 - 50$ mag) it can only be observed in the infrared or at longer wavelengths. Most models for the gas outflow proposed so far assume that it is driven by mass ejection from a young star, namely IRc2 and/or the Becklin-Neugebauer (BN) object which are both very close to the projected center of the mass outflow. IRc2 has a mass-loss rate $\dot{M}_w \approx 10^{-(3...4)} M_\odot \text{ yr}^{-1}$ (Downes et al. 1981) and a luminosity $L_{\text{phot}} \approx 2 \dots 10 \times 10^4 L_\odot$ (Genzel & Stutzki 1989). The mass-loss rate of BN is $\dot{M}_w \approx 4 \times 10^{-7} M_\odot \text{ yr}^{-1}$ and the luminosity $L_{\text{phot}} \approx 1 \dots 2 \times 10^4 L_\odot$ (Scoville et al. 1983).

Another fairly well studied region where formation of stars and their interaction with the ambient medium takes place in an early phase is the Eagle Nebula (M16). Imaging with the WFPC2 onboard the Hubble Space Telescope (Hester et al. 1996) as well as observations in the infrared with ISOCAM (Pilbratt et al. 1998) and NIRSPEC (Levenson et al. 2000) reveal a number of interesting insights into the structure and possible formation history of this active region. The picture of M16 in the optical is dominated by the appearance of the so-called “elephant trunks”, impressive pillars of dense molecular gas protruding into the H II region. Their surface is partly illuminated by the ionizing light of nearby (distance to the pillars ≈ 2 pc) massive stars so that photoevaporative flows from the surface can be identified on the well resolved pictures (Hester et al. 1996) as striations extending normally from the surface of the cloud. The flow is driven by the pressure gradient that arises when the ultraviolet photons from the massive star heat the dense gas at the surface of the trunk to a few thousand Kelvin, resulting in a pressure which is higher than in the rest of the (lower density) H II region.

An interesting question arises in connection with M16: Is the elephant trunk structure a remnant of the original molecular cloud from which the young stars in the region were formed or has this structure actively been molded by the massive stars as a shell swept-up by stellar winds and folded by hydrodynamical instabilities? More detailed observations and better theoretical models are needed to answer this question.

2.4. Previous numerical models of stellar wind bubbles: an overview

Since effects associated with inhomogeneous ambient media or time-dependent stellar parameters as well as the formation of gas dynamical instabilities are difficult to handle within an analytical framework, numerical simulations have become a powerful tool to study the evolution of H II regions and SWBs. First 2D numerical calculations of SWBs have been performed by Różyczka (1985) and Różyczka & Tenorio-Tagle (1985a,b) in a series of papers. For the expansion of the bubble into a homogeneous medium the authors described the formation of clumps in the thin shell but due to the lack of resolution they were unable to completely resolve the dynamics of the shell and to compare it with theoretical predictions. The authors also studied how a change of the wind luminosity (an increase between two fixed levels in a certain time) influences the shell stability and how SWBs break out from a plane-parallel stratified disk. The shell fragmentation as result of an increase of the wind luminosity has also been studied by Stone, Xu, & Mundy (1995) and has been compared with the observation of “bullets” in the vicinity of young stars.

GML1 and García-Segura, Langer, & Mac Low (1996b) focused on the history of the stellar mass loss and the implications for the formation of WR bubbles. They calculated the evolution of the SWB in one dimension until the star enters the LBV phase (for the model with an initial stellar mass of $60 M_{\odot}$) or until the star leaves the RSG stage (for the $35 M_{\odot}$ model). The resulting 1D profiles of circumstellar density, pressure and velocity were used to set up the ambient conditions for 2D calculations of the following stage when the WR wind interacts with the surrounding structure. The authors found that in both cases the slowly expanding shells originating from prior mass loss phases are heavily eroded when they are overtaken by the faster WR wind. This is also the phase in which the resulting nebula shell is considered to be most visible due to the high emission measure in the high density filaments resulting from the collision. The nebula NGC 6888 with its filamentary structure would fit in this picture as being driven by a WR star that has undergone MS and RSG evolution and the shell swept up by the WR wind is currently colliding with the RSG wind shell.

The approach of García-Segura & Franco (1996) is slightly different because they were mainly concerned with the very early evolution of H II regions. They presented 2D gas dynamical calculations for the evolution of H II regions in constant and power-law density profiles and showed the effect of radiative cooling on the thickness of the swept-up shell and therefore also on the development of instabilities. They found that the ionization front can reinforce the growth of the thin-shell instability and in a power-law density fall-off with exponent equal to two it can even lead to violent shell disruption.

Brightenti & D’Ercole (1997) investigated the formation of WR shells resulting from fast

WR winds evolving into slow anisotropic RSG winds. They found that the shell swept up by the WR wind becomes Rayleigh-Taylor unstable and fragments even before it hits the shell that had previously been piled up by the RSG wind. X-ray maps computed from the numerical models show that the anisotropy of the RSG wind leads to a “two-lobe” X-ray morphology which is qualitatively in agreement with the observation of NGC 6888 (Wrigge et al. 1994), but cannot reproduce the small filling factor of the X-ray emitting gas.

Frank, Ryu, & Davidson (1998) tried a different approach: They modeled the interaction of an anisotropic fast wind with an isotropic slow wind to explain the morphology of LBV bubbles. They found that anisotropic fast winds can indeed produce strongly bipolar outflows without assuming that the fast wind collides with a slowly expanding disk or torus as previously postulated.

Strickland & Stevens (1998) calculated simple MS bubbles blown by a wind with constant mass-loss rate and terminal velocity into a uniform ISM. Their main goal was to calculate synthetic X-ray spectra from these numerical models as they would be observed with the ROSAT satellite, in order to analyze these spectra according to standard procedures and to compare the inferred properties with the original numerical models. Surprisingly (or not), they found that the inferred properties of the bubble can considerably deviate from the “real” properties of the model bubble. This implies that detailed X-ray emission models are necessary — instead of simple one- or two-temperature spectral fits — in order to derive reliable properties of bubbles and superbubbles.

In Table 1 we compare the numerical hydrodynamic models of SWBs / H II regions quoted above with respect to the included physics, the covered range of parameters, and some technical properties.

3. Numerical method

3.1. The radiation-hydrodynamics scheme

The numerical calculations presented in this paper have been performed using a 2D radiation-hydrodynamics code with a fairly sophisticated treatment of time-dependent ionization, radiation transfer, and heating and cooling processes. Most features of the code and results of test calculations have already been described in Yorke & Kaisig (1995) and Yorke & Welz (1996). Therefore, here we only give a short summary of the code’s main properties.

The hydrodynamical equations for the conservation of mass, momentum, and energy in an ideal, inviscid, single fluid have been formulated in cylindrical coordinates (r, z) , assuming

axial symmetry around the z axis. This set of equations is solved numerically on an Eulerian grid in the quadrant with $r \geq 0$ and $z \geq 0$, i.e. we additionally assume mirror symmetry with respect to the equatorial plane. The differencing scheme used to discretize the equations is second order accurate in space. Due to operator splitting the accuracy in time is greater than first order. The advection scheme of van Leer (1977) is employed. The star that influences the gas is located in the center of the coordinate system at $r = z = 0$. We use square grids with constant mesh size and insert multiply nested grids in the corner at $r = z = 0$ to enhance the spatial resolution close to the star. All the nested grids are self-similar and the linear spatial resolution is improved by a factor of two for each level of nesting. The basic code is explicit, and therefore the Courant-Friedrichs-Lowy (CFL) condition determines the maximum time step except when changes in the stellar parameters take place on even smaller time scales. Von Neumann-Richtmyer artificial viscosity is used for the treatment of shocks. We use the equation of state for an ideal gas (in our case a mixture of molecular, neutral, and ionized hydrogen with electrons). The formation and dissociation of molecular hydrogen is not yet considered in the energy balance, because it is assumed that continuum radiation below the Lyman threshold dissociates the molecules before the gas is heated up to temperatures where thermal dissociation occurs.

Our integration order starts with the finest grid. The sizes of the time step satisfies the CFL condition for the finest grid as well as for all coarser grids (normalized by the appropriate power of 2). After two time steps have been done on the finest grid and the solution has been advanced to $t + \delta t_1 + \delta t_2$, one time step $\delta t_1 + \delta t_2$ is done on the next coarser grid to advance the solution there to the same time. Because of our prior careful choice of δt_1 and δt_2 , their sum obeys the CFL condition on the next coarser grid. After the solutions on the two grid levels have been advanced to the same point in time, all coarse grid values which have underlying fine grid values (not from the boundary) are replaced by weighted averages from the fine grid. The outer boundary conditions of the fine grid are interpolated from the corresponding grid values of the coarse grid. After this cycle is repeated (taking into account the new CFL time-step constraints) the first integration on the next coarser (3rd level) grid can be performed; 3rd level values are partly replaced by 2nd level values and 2nd level outer boundaries are imposed from 3rd level values, and so on. We use this recursive scheme for 7 grid levels, which means that $\sum_{i=0}^6 2^i = (2^7 - 1) = 127$ single integrations have to be done before one time step on the coarsest grid is completed.

The ionization structure of hydrogen is calculated for each hydrodynamical time step by including the effects of photoionization, collisional ionization, and spontaneous recombination. The absorption of the stellar point-source Lyman continuum by neutral hydrogen is calculated along radial lines-of-sight. We use $N_r + N_z - 1$ rays to ensure that every grid cell is traversed by at least one ray, where N_r and N_z are the numbers of grid cells in r and

z direction, respectively, without ghost cells. The photoionizing radiation field is assumed to have a black body spectrum at the effective temperature of the star. We use the grey approximation for the transfer of the stellar photons, i.e. we calculate the absorption cross section and excess energy only for the mean energy of photons above the Lyman threshold and, therefore, do not account for selective absorption processes. To account for the diffuse Lyman continuum that originates from electron recombinations directly into the ground state of hydrogen we simply use the on-the-spot approximation.

Radiative heating and cooling are considered as source and sink terms in the energy equation and are calculated in an additional substep. Photoionization of hydrogen is responsible for gas heating. The treatment of cooling depends on the gas temperature. Below 15 000 K the contributions by the following processes are explicitly calculated: Bremsstrahlung, collisional ionization of hydrogen, thermal energy lost in hydrogen recombinations, collisional excitation of neutral hydrogen followed by Ly α emission, collisional excitation of the low-lying 1D terms of N $^+$ and O $^{++}$ and the 2D term of O $^+$. Simple assumptions have been made about the degree of ionization of nitrogen and oxygen: Due to the similar ionization potentials and comparable recombination coefficients of H 0 , N 0 , and O 0 , we set the ratios of ionized-to-neutral species for nitrogen and oxygen equal to the respective number calculated for hydrogen, i.e. $\rho_{N^+}/\rho_N = X$ and $(\rho_{O^+} + \rho_{O^{++}})/\rho_O = X$, where X is the hydrogen ionization fraction. It is furthermore assumed that the oxygen ions are equally distributed on the ionization stages O $^+$ and O $^{++}$, i.e. $\rho_{O^+}/\rho_O = \rho_{O^{++}}/\rho_O = X/2$.

The chemical composition is solar everywhere in our computational domain. Helium is not yet considered because it is much less abundant than hydrogen and has no low-lying energy levels. For temperatures above 10 5 K we use the interstellar cooling function from Sarazin & White (1987) with the correction given by Soker (1990). This cooling function is based on the assumption of collisional ionization equilibrium. In the intermediate temperature range between 15 000 K and 10 5 K we calculate both values and use a weighted average. We have not included dust in the calculations presented here.

3.2. Initial conditions

We start all our calculations with the turn-on of the ZAMS stellar radiation field and stellar wind in a homogeneous and quiescent ambient medium. This is definitely a gross oversimplification of what can be expected for the structure of the circumstellar gas shortly after the star has been formed at the end of the pre-MS phase. We have two reasons for our approach: The first is that, in order to understand what happens in the circumstellar medium, it is important to start with a well defined and simple initial configuration. As

we will show below, even with this initially homogeneous ambient density and temperature distribution, the interaction of the SWB with the ionizing radiation field produces a variety of interesting morphological structures whose formation processes have to be understood in detail before studies with a more realistic initial setup can be performed. The second reason is that we want to keep our simulations comparable with those of other authors who use different algorithms or incorporate different physical effects in their codes. We choose $n_0 = 20 \text{ cm}^{-3}$ and $T_0 = 200 \text{ K}$ for our quiescent ambient medium. The density is perhaps high for a star that has already left its parental molecular cloud, but we want to keep our results comparable to those of GML1 who also used $n_0 = 20 \text{ cm}^{-3}$ in order to reduce computational expenses. The temperature $T_0 = 200 \text{ K}$ in the ambient medium was chosen to yield a thermal pressure “typical” for the ISM at the solar galacto-centric distance.

We use a spherical 1D solution after 1000 yr as initial model for the 2D simulations in order to prevent boundary effects from influencing the formation of the very small wind bubble while the development of the self-similar structure is not completed. We switch from 1D to 2D before the swept-up gas collapses into a thin shell that is subsequently subject to instabilities.

3.3. Boundary conditions

In our models the stellar parameters for mass-loss rate (\dot{M}_w), terminal velocity of the wind (v_w), effective temperature (T_{eff}), and photon luminosity in the Lyman continuum (L_{LyC}) are time-dependent boundary conditions which drive and govern the evolution of the circumstellar gas. For the $60 M_\odot$ star we adopt the stellar parameters given by GML1. They were obtained from stellar evolutionary models and from observations and are shown in Figure 2. The $60 M_\odot$ star is supposed to undergo the following evolution: MS O star → H-rich WN star → P Cygni-type LBV → H-poor WN star → H-free WN star → WC star → SN.

According to the mass-loss rate and terminal velocity at time t , appropriate values for density and velocity of the gas are set within the “wind generator region” on the finest grid (a small sphere around the center of the coordinate system where the star is located). The radius of the “wind generator region” is $3.5 \times 10^{17} \text{ cm}$ for the calculations shown in this paper.

Reflecting boundary conditions are used at the r - and z -axis. The outer boundaries of the nested grids were taken from the corresponding values on the next coarser grid. The outer boundaries of the outermost (coarsest) grid are semi-permeable, i.e. mass, energy,

and momentum can flow out of the computational domain, but not in. Of course, outflow would conflict with our intention to carefully take stock of the energetic processes in our calculations. Thus, we prevent outflow by choosing the coarsest grid large enough that neither the ionization front nor moving material can reach the outer boundary before the star dies and the calculation stops.

3.4. Geometry and resolution

The size of the computational domain is $r_{\max} = z_{\max} = 64$ pc. We use 6 nested grids within the coarsest grid, resulting in 7 grid levels. The simulation has been performed with 125×125 cells on each grid level (excluding ghost cells). The linear resolution ranges from 8×10^{-3} pc close to the star to approximately 0.5 pc in the outermost parts of the coarsest grid which were affected only during the late stages of the bubble evolution. For a resolution study we repeat the calculations with 61×61 cells and for the first Myr of evolution with 253×253 cells.

4. Results and discussion

4.1. A resolution study

Before we present our results we briefly discuss their validity. It is currently impossible to spatially resolve all details of the entire dynamical evolution when modeling an SWB in two or more dimensions over such a long time with all the physics we have included. Especially the modes of the thin-shell instability (Vishniac 1983; Ryu & Vishniac 1988; Vishniac & Ryu 1989) are extremely difficult to resolve, because a sufficient number of grid cells across the thin shell is required to follow the tangential flow of material. Mac Low & Norman (1993) performed purely hydrodynamical simulations of the thin-shell instability and confirmed the linear stability analysis of Vishniac (1983). Since they completely focused on the hydrodynamical evolution of the thin shell, they made no efforts to treat much more complex systems with more sophisticated physics.

To check the impact of this resolution effect on our results for the energetic evolution of the SWB, we performed a resolution study. We calculated the same $60 M_{\odot}$ model with three different resolutions, medium (125 cells in each dimension), low (61 cells in each dimension), and high (253 cells in each dimension). We compare only the first Myr of the evolution (because the high-resolution model is too CPU intensive). The results are displayed in Figure 3. The change of kinetic energy due to different resolutions is systematic (at times

later than 0.2 Myr) in the sense that a higher resolution increases the kinetic energy that remains in the system. For most of the time the difference in kinetic energy between medium and high resolution ($\lesssim 0.05$ dex) is smaller than between low and medium resolution, which is expected as the value converges toward the limit. The variation of the thermal energy with resolution is only weak, the maximum difference between low and high resolution is $\lesssim 0.05$ dex at any time during the first Myr. The scatter in ionization energy for the three different resolutions is also $\lesssim 0.05$ dex for $0.5 \text{ Myr} \leq t \leq 1.0 \text{ Myr}$ and $\lesssim 0.1$ dex for $t < 0.5 \text{ Myr}$. In the latter case, the deviation of ionization energy between the medium and high resolution runs varies, but is considerably smaller than between low and medium resolution, indicating that the value of the ionization energy is already close to the actual value.

These results show that the errors in our energetic analysis due to resolution effects are within an acceptable range, although some details of the evolution are not yet completely resolved in our calculations.

4.2. The evolution of the $60 M_{\odot}$ model

Figures 4 to 16 show the evolution of the circumstellar gas around our $60 M_{\odot}$ model star. The plots show grey-scale coded physical quantities in a quadrant of the r - z -plane through the star. The size of the displayed area varies with time as the expansion proceeds outward. The star is located in the center of the coordinate system. We display the mass density together with the velocity field, the gas temperature, and the degree of hydrogen ionization, respectively, for certain stages of evolution. The degree of ionization is not shown for stages after 1 Myr, when the ionized region spatially almost coincides with the hot gas. To prevent confusion, velocity arrows are skipped in the free-flowing wind and (except for Figure 4) in the hot bubble.

Figure 4 shows the initial model for the 2D calculation that has been set up from the 1D solution after 1000 yr. The fundamental structure of the combined SWB / H II region is well described by the analytical solutions. The ionization front at a distance of about ≈ 8 pc from the star separates the ionized gas at about 8000 K from the undisturbed medium. The front has not yet reached the initial Strömgren radius at about 12.7 pc and is still R-type. Thus, there is little dynamical response of the heated gas at this point. The SWB evolves into the pre-ionized and pre-heated but otherwise undisturbed medium. The free-flowing wind is heated by the reverse shock at $r \approx 0.16$ pc to very high temperatures of about 10^8 K. Though the density in the hot gas is fairly low ($\approx 4 \times 10^{-25} \text{ g cm}^{-3}$), the thermal pressure is still much higher than in the H II region and the hot bubble expands supersonically (with respect to the isothermal sound speed in the H II region of $\approx 12 \text{ km s}^{-1}$) at roughly 200 km s^{-1} . The

photoionized H II region gas becomes shocked by the expanding hot bubble and compressed into a shell with a density of more than $10^{-22} \text{ g cm}^{-3}$ and a temperature of nearly 10^6 K . At this early time, the SWB and the photoionized H II region still evolve independently.

Figure 5 depicts the evolution after $2 \times 10^4 \text{ yr}$. The photoionized region has reached its initial radiative equilibrium size and gas at the outer edge of the H II region starts to accelerate outward due to the pressure gradient between the warm ionized gas and the cold neutral ambient medium. The hot bubble has grown to about 2 pc in radius. The shell has been decelerated to approximately 60 km s^{-1} . Due to the high density and high temperature, strong cooling has led to compression of the swept-up gas into a thin shell. The thin-shell instability initially produces some dense knots in the shell that imply variations in the optical depth along radial lines-of-sight indicated by the rippling of the photoionization front. The initial evolution of the SWB (as long as it is independent of the H II region evolution) is very similar to what is described by Strickland & Stevens (1998), except for the deviations due to the different ambient density and stellar parameters.

On the basis of Figure 6 ($t = 4 \times 10^4 \text{ yr}$) and Figure 7 ($t = 0.1 \text{ Myr}$) the structuring impact of the interaction processes between the SWB and the H II region can be well identified: The photoionized H II region has started to expand into the ambient medium at 6 to 7 km s^{-1} . The isothermal sound speed of the cold neutral gas is about 1 km s^{-1} . Thus, an outer radiative forward shock occurs that sweeps up the ambient gas into a shell. The hot gas bubble has grown to about 5 pc in radius and the shell expansion velocity is still about 25 km s^{-1} ($t = 0.1 \text{ Myr}$). The ionization plots nicely illustrate the influence of the density knots in the wind bubble shell on the evolution of the H II region: The gas clumps cast shadows into the H II region. The optical depth for hydrogen ionizing photons along lines-of-sight through the clumps is higher than for lines-of-sight which pass the shell between clumps. Due to the weakening of the radiation field, the gas behind the clumps starts to recombine, forming neutral spokes within the H II region. The spokes are less prominent in temperature than in degree of ionization, because the cooling efficiency breaks down with the disappearance of the free electrons and the shadowed regions remain at several thousand K for some time.

One could imagine that the shadowed regions are artificial due to the use of the on-the-spot approximation for the diffuse radiation field that originates from recombinations directly into the ground state of hydrogen. But a test calculation that used flux limited diffusion instead of the on-the-spot approximation yielded qualitatively the same results with respect to the shadowed regions. Only slight morphological differences were obtained due to the transfer of the diffuse radiation field.

Considerations about the influence of shadow patterns on ionized regions are not com-

pletely new: Capriotti (1973) already discussed the impact of shadows by shell fragments on the formation and appearance of planetary nebulae (PNe). Williams (1999) examined the corrugation of R-type ionization fronts by density inhomogeneities with subsequent formation of dense clumps. Soker (1998) studied the formation of compressed tails in the shadow zones behind dense clumps which are present in the vicinity of the central star of a PN before the ionization starts. And Cantó et al. (1998) presented an analytical model for the partial ionization of the shadow regions behind neutral clumps by the diffuse radiation produced in the nebula along with some gas dynamic simulations. The model is not restricted to PNe and can be generalized to photoionized regions.

Richling & Yorke (2000) considered the effects of UV dust scattering and calculated the evolution of disks externally illuminated by an O star. Here, also, shadows are cast which appear cometary in shape with tails pointing away from the ionizing source. Had we considered UV scattering by dust in this investigation it is very likely that our clumps' shadows would also have had a cometary shape.

For the combined H II region / SWB described in our work we show that the density inhomogeneities needed to cast the shadows can be produced by the action of the stellar wind even after the H II region has already been formed in a completely uniform medium. In our case the growth of the ionized fingers of the H II region is therefore not only due to the ionization front instability described by García-Segura & Franco (1996). It is strongly triggered by the redistribution of mass (and thus opacity) by the action of the stellar wind shell.

The real nature of the spokes, clumps, and instabilities is 3D rather than 2D, a fact which certainly should influence their size distribution, shapes, and longevity. 3D simulations, though extremely expensive, would be useful to study these structures in more detail. These 2D simulations should thus be regarded as qualitative indicator that such instabilities exist, a feature missing from 1D calculations.

Another consequence for the structure of the H II region and the shell of the SWB can be seen on Figure 8 at 0.22 Myr. The disturbed structure of the H II region, especially the formation of the neutral spokes and the ionized fingers, has induced several flow patterns with velocities up to $\approx 20 \text{ km s}^{-1}$. Due to the pressure gradient between the neutral spokes and the ionized gas, the spokes are compressed by the ionized gas. At the same time the expanding SWB compresses the H II region (and its spokes) as a whole. The clumps in the stellar wind shell originally responsible for the shadows grow in mass and partially merge during the further course of evolution. Photoevaporation of the stellar wind shell and its embedded clumps does not strongly influence the dynamics, because the gas in these structures is still warm and its photoionization does not produce large pressure gradients. However, where

stellar photons directly impinges upon the cold outer shell through the optically thinner ionized fingers photoevaporation occurs and leads to significant dynamical effects, as evident in Figures 8 through 16.

In the top panel of Figure 8 and also in some of the other density plots are swirls of material visible in the hot bubble. These vortices are sometimes generated at the r - and z -axes, possibly as an artifact of the reflecting boundary conditions. Since the total mass involved in these flow patterns is very small, they do not influence the morphological or the energetic evolution significantly.

Proceeding to 0.5 Myr (Fig. 9, note the different scale) we see that the entire H II region has been swept up by the SWB, which has grown to approximately 12 pc in radius. The photoionized H II region (it can best be distinguished from the hot bubble using the temperature plot) consists of 3-7 pc long pillars, the remnants of the ionized fingers. The stellar wind shell loses its structure, becomes more or less dissolved, and merges into the “remnant” H II region, because it sweeps up a highly nonuniform medium with an expansion speed that becomes comparable to the sound speed of the H II gas.

Figures 10 and 11 compare the results of our high and medium resolution runs with respect to the morphological structure after 1 Myr. One can easily see that there are significant deviations in the structure of the photoionized region between the two runs. This is not very surprising, because, as mentioned above, the formation of density fluctuations due to the thin-shell instability is very sensitive to the spatial resolution, especially as we have started with a completely undisturbed ambient medium and have not artificially excited any particular unstable mode. And we have also seen that exactly these clumps in the stellar wind shell strongly influence the evolution of the H II region due to their opacity for Lyman continuum radiation.

Nevertheless, the general structure is very similar for both resolutions: The radius of the hot bubble is roughly 17 pc (strong deviations from spherical shape appear in both cases). The photoionized gas forms a highly irregular shell around the hot bubble with a mean thickness of ≈ 5 pc, bound on the outside by a swept-up shell of shocked ambient material. It appears as if the phenomenon of “break-out” of the hot gas into the photoionized gas has occurred between the spokes in both cases. However, we see no evidence for further break-out into the undisturbed constant density medium. Had we chosen an ambient environment of limited size — i.e. included cloud edges of decreasing density within the computational grid — we could expect a more dramatic demonstration of break-out.

We now jump to $t = 3.30$ Myr and show in Figure 12 the evolutionary state of the circumstellar material shortly before the star enters the LBV phase with its strongly enhanced

mass-loss rate. (Please note that we once again changed the plot scale to an appropriate size.) The radius of the hot bubble has grown to approximately 40 pc. Due to the growth of the bubble (and the slight decrease of H-ionizing photon luminosity after 2 Myr) the photoionized H II region has more or less collapsed into a skin with ≈ 2 pc thickness at the inside of the outer shell. The outer shell itself is still corrugated, and so is the photoionized gas. Some small clumps have become detached from the shell.

Figure 13 depicts the structure during the LBV eruption. Compared with the earlier plots one can detect a much higher density in the free-flowing wind zone. That is due to the higher mass-loss rate of the star and the smaller terminal velocity. The rest of the structure is largely unchanged, because the time-step difference is small.

The LBV phase lasts only for about 10 000 yr and is followed by the final WR phases of the star, which are once again associated with wind terminal velocities of a few 1000 km s^{-1} . GML1 describes what happens next: The WR wind becomes shocked when it hits the much slower LBV wind and the hot, rarefied gas accelerates the dense LBV wind (Fig. 14). This is now a highly Rayleigh-Taylor unstable situation and the shocked WR wind breaks through the LBV material, fragments it, and blows it into the MS bubble (Fig. 15) where it mixes with the hot, rarefied gas, enhancing the density and lowering the temperature there for some time.

The last set of pictures (Fig. 16) shows the structure of the circumstellar gas at the end of our simulation. This is the pre-SN configuration immediately before the star explodes as SN II. The radius of the hot bubble has reached nearly 50 pc and the photoionized H II region is limited to the illuminated inner skin of the outer shell of swept-up ambient gas.

A “re-ionization” phase (cf. Beltrametti, Tenorio-Tagle, & Yorke 1982; Tenorio-Tagle et al. 1982) cannot be found in our model, because the dynamical evolution of the circumstellar gas at late stages is dominated by the influence of the stellar wind rather than the stellar radiation field.

4.3. The energy balance in the circumstellar gas

4.3.1. Numerical results

Figure 17 shows the total energy contributions in the circumstellar gas of the $60 M_\odot$ model as a function of time. We follow the kinetic energy of bulk motion throughout the computational domain, the ionization energy (13.6 eV per ionized hydrogen atom), the thermal energy of cold ($T \leq 10^3 \text{ K}$), warm ($10^3 \text{ K} < T < 10^5 \text{ K}$), and hot ($T \geq 10^5 \text{ K}$) gas. As

we have seen before, the ionization and heating of the H II region is the fastest process at the beginning of the evolution. Thus, the ionization energy reaches 1.1×10^{50} ergs and the thermal energy of warm gas around 1.5×10^{49} ergs very soon after the stellar turn-on.

The evolution of the thermal energy of warm gas follows that of the ionization energy over the lifetime of the star with a shift of 0.7-0.9 dex. This is due to the fact that photoionization by the stellar radiation field is responsible for the bulk production of ionized gas at typically 8000 K. The contribution by shock heating is small, because the reverse shock does not heat much mass and the thermal energy of this gas is accounted under “hot gas” rather than “warm gas”. Therefore, we will discuss only the ionization energy bearing in mind that the thermal energy of warm gas behaves quite similarly.

An interesting feature is the drop of ionization energy between its first maximum and $t \approx 0.2$ Myr. This is due to the formation of the dense structures (shell, spokes) in the H II region which reduce the recombination time and increase the cooling of the gas (see also Fig. 18). Between $t \approx 0.2$ Myr and $t \approx 1.9$ Myr the denser structures dissolve and the pressure decay within the hot bubble together with the H II region expansion result in a decrease of density in the H II region. Thus, the recombination time increases and the ionization energy stored in the system increases accordingly. The ionization energy reaches 2.7×10^{50} ergs and the thermal energy of warm gas 3.7×10^{49} ergs.

As the star enters the first WN stage at $t \approx 1.7$ Myr, the photon luminosity in the Lyman continuum begins to decrease slightly while the mechanical wind luminosity starts to increase (see Fig. 2). The former directly reduces the rate of photons available for photoionization, whereas the latter enhances the pressure in the hot bubble, thus compressing the H II region, which implies higher recombination rates. Thus, ionization energy and thermal energy of warm gas decrease by a factor of 2 and reach local minima at $t \approx 2.6$ Myr. They rise again when the photon luminosity in the Lyman continuum increases and the mechanical wind luminosity decreases until the star reaches the LBV stage.

Though spectacular in appearance, the impact of the LBV phase on the energy balance is only limited due to a relatively brief period of time. We note here that the table of stellar parameters that we use is sufficiently time resolved even during the LBV phase, contrary to what could be suspected from Figure 2. For a detailed plot of the stellar parameters during the LBV phase see GML1. The ionization energy in the circumstellar gas drops during the LBV stage, because the effective temperature of the star decreases significantly. But immediately after the LBV eruption during the next WN stage the stellar UV flux drives the circumstellar ionization energy to a global maximum at 3.4×10^{50} ergs. The ionization energy follows the stellar UV flux. The final values of ionization energy and thermal energy of warm gas (i.e. at the end of our calculation) are 1.0×10^{50} ergs and 2.1×10^{49} ergs,

respectively.

The kinetic energy of bulk motion in the circumstellar gas rises from zero at the beginning (because we started with a quiescent medium) as more and more circumstellar gas is accelerated by the expansion of the H II region and the SWB. After some 0.3 Myr it reaches the same level as the thermal energy of warm gas and rises in the same manner. When the mechanical luminosity of the stellar wind increases in the first WR phase it lifts the kinetic energy above 10^{50} ergs, close to the ionization energy level. The ejection of the LBV nebula raises the kinetic energy for a short time almost by a factor of 2, but it drops back when the LBV material hits the outer shell and the kinetic energy is dissipated into thermal energy. Its final value is 1.4×10^{50} ergs.

The thermal energy of hot gas accounts for the internal energy of the rarefied gas in the SWB that is heated to high temperatures by the reverse shock during the MS and WR phases of the star. Since there is no hot gas at the very beginning, the thermal energy of this gas phase rises from 0. The behavior of the curve is very similar to that of the kinetic energy but it increases faster during the first WN stage of the star. Between 2.3 and 3.1 Myr it is the dominant form of energy in our system and after some slight changes in and around the LBV phase it finally decays with the mechanical luminosity of the star to 9.7×10^{49} ergs.

The thermal energy of cold gas starts already with the internal energy of the quiescent ambient medium. The value increases smoothly from 3.4×10^{49} ergs at the beginning to 7.9×10^{49} ergs at the end of the calculation, because more and more ambient gas becomes swept up by the outer shell. The weak shock heats it to several 100 K whereas cooling of this neutral gas is very low.

At the beginning the radiative energy input has the strongest influence on the energy distribution. The dynamical response of the circumstellar gas (the expansion of the H II region and the acceleration of the material by the SWB) takes much longer. Thus, the ionization energy dominates the circumstellar energy distribution over the first ≈ 2 Myr. After the kinetic energy and thermal energy of hot gas have caught up with the thermal energy of warm gas, these three forms of energy are comparable between 0.3 and 1.8 Myr. Later, due to the accumulation of kinetic energy in the shell and thermal energy of hot gas in the bubble, these two become comparable with the ionization energy. Between 2.2 Myr and the end of the calculation these three forms of energy differ by not more than a factor of 3, though some changes occur. The LBV phase of the star induces very rapid changes in the relative energy ratios of at most a factor of 3 but they are transitory.

It is interesting to compare the energy stored in the system for the two cases: 1) with wind and 2) the pure H II region evolution without wind (Fig. 18). Obviously, the total kinetic

energy in the calculation with wind is always higher than in the corresponding calculation without, because of the added kinetic energy of the SWB shell. At the end of the calculation, the kinetic energy in the model with stellar wind is 4 times higher than in the model without.

By contrast, the ionization energy reaches the same level of $\approx 1.1 \times 10^{50}$ ergs very soon after the start of the calculation in both cases. As we have already seen in Figure 17, the ionization energy in the model with wind drops by a factor of 2 during the first 0.2 Myr whereas in the model without wind it continues to grow. This supports our explanation that inhomogeneities in the H II region (shell, spokes) result in shorter recombination times and thus lead to fewer photoionized hydrogen atoms in the system. Although there is additional energy input by the stellar wind, the ionization energy is lower than in the calculation without wind by 0.1 to 0.4 dex for most of the evolution. This, however, does not imply that the H α luminosity is different. The H α luminosity directly mirrors the stellar ionization input.

Although the thermal energy of warm gas (55 % below the respective value of the windless model at the end of the calculation) is similarly affected as the ionization energy, the total thermal energy is always higher in the model with wind, because we have additional energy deposited into the hot and into the cold gas phases.

Whereas the mechanical power of the stellar wind and the radiative power of the star are the energy sources in our system, the only energy sink term is radiative cooling of the gas. All other energetic processes lead to a redistribution of forms of energy within the system but not to a change of the total energy. Figure 19 shows the total energy loss of the system due to cooling of the gas and distinguishes 3 different contributions: “H ionization loss” refers to the 13.6 eV binding energy per hydrogen recombination into all states above the ground state, while “H thermal loss” accounts for the thermal energy of the electrons lost by the same process. “Other processes” include all other cooling processes considered such as collisionally excited line emission and Bremsstrahlung. One can see from Figure 19 that the shape of all the curves follows the Lyman continuum photon luminosity of the star (see Fig. 2). The total energy-loss rate during the MS phase is close to 10^{39} ergs s $^{-1}$, approximately the same as the stellar Lyman continuum luminosity. Although the ionization energy in the system rises to 10^{50} ergs during the first few 10 000 yr, it is only a small fraction of the total input energy.

“H ionization loss” is the dominant energy sink term during the evolution. It accounts for roughly 80 % of the total emitted power during the MS and first WN stage of the star. After the LBV phase, the relative importance of “other processes” has risen because the LBV ejecta enhanced the density in the hot bubble where collisionally excited lines and Bremsstrahlung dominate the energy emission.

Figure 20 shows the transfer efficiency into kinetic, ionization, and thermal energy and their sum for the model without wind. We define the transfer efficiency as the cumulative fraction of the input energy that has been converted into a particular form up to the time $t = \tau$. In this case we have only radiative input energy and all values are related to that.

The transfer efficiency into ionization energy has the highest value during the whole calculation. The transfer efficiencies into ionization and thermal energy strongly drop at the beginning of the calculation. This is a consequence of the fact that the photoionization equilibrium has been quickly established and the ionization energy stays constant within an order of magnitude, whereas the transfer efficiency is related to the accumulated input energy that grows continuously in time. The transfer efficiency into ionization energy reaches $\approx 5 \times 10^{-3}$ immediately before the LBV phase and drops due to the decreasing photon luminosity in the final WR phases by almost a factor of 5. The transfer efficiency into thermal energy reaches the level of 10^{-3} before the LBV phase, but decreases only by less than a factor of 2 during the remaining evolution. The discrepancy between the declines of both values can again be explained by the fact that cooling in formerly photoionized gas is greatly reduced due to missing electrons after recombination occurs. Thus, the recombined neutral gas has lost all its ionization energy but can retain a considerable portion of its thermal energy over a relatively long period. The transfer efficiency into kinetic energy has reached a nearly constant level of $\approx 3 \times 10^{-4}$ after 1 Myr and remains at that level until the end of the calculation, i.e. after the first Myr the kinetic energy in the system grows almost proportionally to the total input energy.

Now we check the impact of the stellar wind on the energy transfer in the system. Figure 21 shows the same transfer efficiencies as Figure 20 but for the model with wind and radiation. Whereas for the model without wind the transfer efficiency into ionization energy dominated the total energy transfer efficiency, for the model with wind this is only true during the first ≈ 2.2 Myr. In the first WN phase the transfer efficiency into thermal energy dominates for about 1 Myr, because the photon luminosity in the Lyman continuum decreases and the mechanical wind luminosity increases, thus enhancing the production of hot gas. Curiously, in the LBV phase all three energy transfer efficiencies have the same value of about 2×10^{-3} . As in the case without wind, the transfer efficiency into ionization energy drops more strongly after the LBV phase than that into thermal energy. The drop of the latter one in this model is mostly due to energy loss of the hot gas that dominates the thermal energy at late stages of the evolution.

The total energy transfer efficiency reaches approximately 4×10^{-3} at the end of the calculation, about twice as much as in the model without wind. This is interesting, because we know from Figure 2 that the mechanical wind luminosity integrated over the whole

lifetime of the star is almost negligible compared to the total radiative energy input in the Lyman continuum. In other words, although the stellar wind itself does not actually inject a considerable amount of energy into the circumstellar gas (compared to the stellar radiation field), its presence almost doubles the total energy that is finally contained in the gas. This difference is due to the fact that the thermal energy deposited increased by a factor of 2.4 and that the kinetic energy rose by a factor of 4 compared to the model without wind. The ionization energy actually decreased slightly by some 20 – 30 %.

To facilitate the discussion in the next section we summarize the values of the individual energy components at the end of the simulation in Table 2. Besides the kinetic energy of bulk motion (E_k) and the ionization energy of hydrogen (E_i) we list the thermal energy of the cold, warm, and hot gas components ($E_{t,\text{cold}}$, $E_{t,\text{warm}}$, and $E_{t,\text{hot}}$) for the two models, one with and one without stellar wind. The values of the energy transfer efficiency into kinetic energy (ε_k), ionization energy (ε_i), and thermal energy (ε_t) at the end of the simulation are given in Table 3. The total energy of the Lyman continuum radiation emitted by the star is $E_{\text{LyC}} = 1.07 \times 10^{53}$ ergs and the mechanical energy injected into the system by the stellar wind, if considered, amounts to $E_w = 3.31 \times 10^{51}$ ergs.

4.3.2. Comparison with analytical results

We now calculate the values for the kinetic-, ionization- and thermal energy in the system according to the analytical solutions given in section 2. The analytical approach cannot handle time-dependent stellar parameters, therefore we simply choose mean values for effective temperature and luminosity in the Lyman continuum over the lifetime of our model star. With $\langle T_{\text{eff}} \rangle = 5.03 \times 10^4$ K, $\langle L_{\text{LyC}} \rangle = 8.33 \times 10^{38}$ ergs s⁻¹, and using $\alpha_B = 3.37 \times 10^{-13}$ cm³ s⁻¹ as hydrogen recombination coefficient and $c_{s,\text{II}} = 1.15 \times 10^6$ cm s⁻¹ for the isothermal sound speed in the H II region (corresponding to $T_{\text{II}} = 8000$ K), we obtain for $n_0 = 20$ cm⁻³ after $\tau = 4.065$ Myr from equations (3), (4), and (5) for the model without wind:

$$\begin{aligned} E_k &= 4.3 \times 10^{49} \text{ ergs ,} \\ E_i &= 5.0 \times 10^{50} \text{ ergs ,} \\ E_t &= 7.7 \times 10^{49} \text{ ergs .} \end{aligned}$$

The energy transfer efficiency in the analytical approach is then defined as

$$\varepsilon = \frac{E}{\tau \langle L_{\text{LyC}} \rangle} , \quad (11)$$

where E can be any of E_k , E_i , and E_t , depending on the efficiency that is calculated. Thus, we obtain

$$\begin{aligned}\varepsilon_k &= 4.0 \times 10^{-4}, \\ \varepsilon_i &= 4.7 \times 10^{-3}, \\ \varepsilon_t &= 7.2 \times 10^{-4}.\end{aligned}$$

Bearing in mind all the assumptions and approximations which have been made to obtain the analytical expression for the kinetic energy of bulk motion (see Lasker 1967), the deviation of less than 30 % in ε_k is not too bad. This difference is not due to the constant effective temperature and luminosity that we have chosen to obtain the analytical result. Recalculating ε_k for the first Myr, where the stellar parameters are about constant, makes the discrepancy between the analytical and numerical value of ε_k even larger. The difference is more likely due to temperature deviations from 8000 K in the H II region of the model calculation.

Comparing the analytical and numerical results for the transfer efficiency into ionization energy shows fairly good correspondence immediately before the LBV phase. At the end of the calculation the numerically determined transfer efficiency is about 0.6 dex below the analytical value because the Lyman continuum luminosity of the star drops significantly during the final WR phases of the star and the ionization energy follows immediately. Of course, the analytical solution cannot reproduce this feature. The correlation between the drop of Lyman continuum luminosity and the thermal energy is weaker, because cooling ceases when the plasma becomes neutral, as already mentioned above. Thus, the correspondence between analytical and numerical transfer efficiency into thermal energy is much better and the deviation at the end of the calculation is less than 15 %.

It is more difficult to compare analytical with numerical results in the case of the combined H II region / SWB model because we have only the analytical energy transfer efficiency solutions for the H II region and SWB separately. We simply add up the energy contributions from the H II region and the SWB bearing in mind that this is only a rough approximation, which actually neglects the interactions between both structures. Because we have not considered cooling in the hot bubble, the analytical energy transfer rates into kinetic and thermal energy are upper limits.

We insert the mean value of the mechanical wind luminosity, $\langle L_w \rangle = 2.58 \times 10^{37} \text{ ergs s}^{-1}$, into equations (9) and (10) and together with the results for the pure H II region we obtain

$$\begin{aligned}E_k &= 9.5 \times 10^{50} \text{ ergs}, \\ E_i &= 5.0 \times 10^{50} \text{ ergs},\end{aligned}$$

$$E_t = 1.6 \times 10^{51} \text{ ergs .}$$

To find the energy transfer efficiency, we relate these values to the sum of Lyman continuum radiation energy and the mechanical wind energy (which, of course, is almost negligible),

$$\varepsilon = \frac{E}{\tau (\langle L_{\text{LyC}} \rangle + \langle L_w \rangle)} , \quad (12)$$

where E can again be any of E_k , E_i , and E_t . We get

$$\begin{aligned} \varepsilon_k &= 8.6 \times 10^{-3} , \\ \varepsilon_i &= 4.6 \times 10^{-3} , \\ \varepsilon_t &= 1.4 \times 10^{-2} . \end{aligned}$$

We have already discussed the fact that the ionization energy in the numerical model with wind is lower than in the model without wind. This slightly enhances the discrepancy between the analytical and the numerical results for the ionization energy in the case with stellar wind. On the other hand, there is no indication that the neglect of the ionization energy in the hot bubble is a bad approximation.

The increase of the thermal energy deposit from the windless H II region model to the combined SWB/H II region model (factor 2.4) is almost an order of magnitude below the analytical upper limit. Since the conversion of thermal energy by PdV work is the major source of kinetic energy, the increase of the kinetic energy deposit between the models without and with wind (factor of 4 at the end of the calculation) is also 82% below the analytical upper limit. These findings are supported by the observation that the radius of the bubble at the end of the calculation (≈ 50 pc) is considerably smaller than the analytical result of ≈ 68 pc according to equation (6). One reason for the lack of thermal energy in the numerical model is the variation of the mechanical luminosity of the star. The LBV wind enhances the density in the bubble which leads to stronger cooling, and the mechanical luminosity of the stellar wind generally decreases during the last 0.6 Myr. But also during the other stages of evolution, cooling in the hot bubble is not completely negligible for the energetics of the system. The thermal energy of the hot bubble calculated analytically at $t = 1$ Myr is already a factor of 4.5 larger than the corresponding value in the numerical model. Although we have not implemented heat conduction, effects like turbulent mixing between hot and cold gas as well as numerical diffusion enhance the cooling rate. The resolution dependent numerical diffusion is not a key factor as we have shown in our resolution study. However, the cooling due to gas mixing is enhanced because the SWB expands at the beginning into the highly nonuniform H II region, a fact that cannot be properly handled by the analytical description. In general, the analytical results for the upper limits of the transfer efficiency into thermal and thus kinetic energy of bulk motion are much higher than the values from the numerical simulations even without heat conduction.

4.4. Direct observational implications

Finally, we briefly discuss some direct observational implications of our models. Since for a correct construction of intensity maps one would need 3D models, the results of our 2D calculations can only give a rough estimate of the observable intensities. Thus, we have calculated angle-averaged intensity profiles for H α and soft X-ray emission based on the cylindrical symmetry in our models.

The H α emissivity is calculated according to the table (case B) in Osterbrock (1989). We use a $T_{\text{II}}^{-0.92}$ fit for the temperature dependence and set the emissivity to zero where the degree of hydrogen ionization is below 10^{-4} . We do not account for absorption.

In Figure 22 we plot the angle-averaged H α intensity profiles at two different times ($t = 0.22$ Myr, during which intense structure formation occurs in the H II region, and $t = 3.365$ Myr, at a late stage after the LBV phase of the star). For comparison, we have also plotted the H α intensity profiles of the corresponding models without stellar wind for the same times.

At $t = 0.22$ Myr the pure H II region model without stellar wind shows the intensity profile of a spherical, emitting volume that has just started to expand. On the other hand, the intensity profile of the model with stellar wind shows a dominant peak between $r = 8$ and 9 pc. This peak represents the global intensity maximum at that time and is produced by the emission of the dense shell swept up by the hot bubble of shocked stellar wind gas. A secondary, much smaller peak between $r = 13$ and 14 pc originates from the trapping of the ionization front in the dense outer shell fragments piled up by the expanding H II region.

Comparing these data with the intensity profiles at $t = 3.365$ Myr shows that the further expansion of the bubble and H II region generally lowers the H α surface brightness, as expected for comparable Lyman continuum fluxes. In particular, when the SWB completely overtakes the H II region and enlarges the whole structure, the H α surface brightness is lower than in the pure H II region model at the same time.

Due to the facts that the photoionized region is more or less limited to the illuminated inner part of the shell and that the H α emissivity in the hot cavity is very low, the intensity profile of the combined SWB / H II region appears slightly limb brightened. The H α emission from the WR bubble is barely visible above the H α background from the MS bubble. It might be that in our simulation the shell of the WR bubble is too hot (e.g. due to the neglect of heat conduction) and thus emits more strongly in X-rays (see below) than in the optical.

For the X-ray intensity profiles in the energy range from 0.5 keV to 3.0 keV we use the emissivity calculated with the Raymond & Smith (1977) program for cosmic chemi-

cal composition (Allen 1973). The emissivity is set to zero for temperatures below 10^5 K; absorption is not considered. In Figure 23 we display the angle-averaged soft X-ray intensity profiles at $t = 1.0$ Myr, 3.30 Myr (before the LBV-phase), and 3.365 Myr (after the LBV-phase). The two snapshots before the LBV stage show intensities between 10^{-10} and 10^{-8} $\text{ergs s}^{-1} \text{cm}^{-2} \text{sr}^{-1}$ for lines of sight through the hot bubble. After the LBV stage, the soft X-ray intensity close to the center of the bubble is strongly enhanced by more than three orders of magnitude to values above 10^{-6} $\text{ergs s}^{-1} \text{cm}^{-2} \text{sr}^{-1}$ when the shocked WR wind hits the LBV ejecta. The soft X-ray emission comes mainly from the inside of the shell of the swept-up LBV wind, before it breaks apart.

The WR nebula RCW 58 around HD 96548 (= WR 40) is a possible candidate for an observed counterpart of the WR nebula that forms in our model calculation at $t = 3.365$ Myr. The WR star is currently of type WN8 and there are indications that the star passed the LBV stage (GML1; Humphreys 1991). The mean radius of the optical nebula is 3.5 pc (Chu 1982) or 2.5 pc (Arthur et al. 1996) depending on the estimation of the distance to HD 96548. Thus, the evolutionary state of the nebula should be approximately comparable to the nebula in our model.

Though the strong increase of the surface brightness in our model after the LBV phase is basically in agreement with the fact that up to now only WR bubbles (and no MS bubbles) have been observed in X-rays, the comparison with RCW 58 shows that our model also suffers from the same problem that all analytical and numerical models thus far have: The X-ray luminosity is much higher than observed. In our model, the X-ray luminosity of the WR bubble in the energy range from 0.5 keV to 3.0 keV is 7×10^{33} ergs s^{-1} whereas Moffat et al. (1982) report that no X-ray emission from RCW 58 was detected with the EINSTEIN satellite, meaning the X-ray luminosity of RCW 58 in this energy range must be below 10^{32} ergs s^{-1} (Arthur et al. 1996).

4.5. The impact of the ambient medium, the stellar parameters, and unconsidered physics

Due to the immense computational efforts we can only show results for one set of ambient medium parameters ($n_0 = 20 \text{ cm}^{-3}$ and $T_0 = 200 \text{ K}$). We shall utilize the scaling laws for H II regions in ionization/recombination and heating/cooling equilibrium with negligible gravity (see table 2 of Yorke et al. 1982) and briefly discuss the changes of the results that we expect if other values for the ambient medium are used. Separating the evolution of the H II region and SWB, we note that if the density in the ambient medium is modified by a factor $\tilde{\delta}$ while assuming the same equilibrium temperature and same ionizing luminosity, all linear scales

$\tilde{\lambda}$ and time scales $\tilde{\tau}$ transform according to $\tilde{\lambda} \propto \tilde{\tau} \propto \tilde{\delta}^{-2/3}$, velocities remain unchanged, and mass outflow rates and mechanical luminosity (as well as other rates of energy changes) transform as $\tilde{\delta}^{-1/3}$. Values for the various energies given at a particular time scale as $\tilde{\delta}^{-1}$. Thus, an increase in ambient density results in smaller H II regions, lower energy injection rates and proportionally lower values for the ionization, thermal, and kinetic energy. These same scaling laws can be derived in a less rigorous manner from our equations 2 to 5.

Modifying the temperature of the ambient medium does not strongly affect the evolution as long as the gas is not ionized and the pressure in the H II region is much higher than the pressure of the ambient medium.

With respect to the SWB, equation 6 shows that the radius of the SWB is proportional to $\rho_0^{-1/5}$, i.e. at comparable times it is smaller (larger) by $\tilde{\delta}^{1/5}$ in the case of an ambient density higher (lower) by a factor $\tilde{\delta}$. In contrast to the H II region, the growth of the thermal and kinetic energy of the SWB does not depend on the ambient density, as long as the assumptions under that equations 9 and 10 were derived remain fulfilled (e.g. thermal pressure in the hot bubble is much higher than the thermal pressure in ambient medium).

It is difficult to estimate the impact of a variation of the ambient conditions on the highly non-linear H II region / SWB interaction effects. Basically, an increase of the density in the ambient medium leads to both a smaller SWB and a thicker shell of swept up material. Thus, the ratio of shell thickness to SWB diameter grows which increases the unstable length scales and tends to inhibit thin shell instabilities with all their associated effects. On the other hand, clumpiness in the circumstellar medium may exist anyway, abolishing the need to trigger the interaction effects by shell instabilities. It is clear that numerical simulations under a variety of different ambient conditions are highly desirable in order to study these effects in more detail. They will become available with increasing computer power.

It should also be noted here that the stellar parameters which we use as time-dependent boundary conditions in our simulations are still somewhat uncertain. E.g. Martins, Schaerer, & Hillier (2002) showed that the determination of the effective temperature of O dwarfs based on non-LTE line blanketed atmosphere models including stellar winds results in differences to previous calibrations up to a few 1000 K. The mass-loss rate and its temporal variation in the short and violent evolutionary stages like the LBV phase are probably even less well known. We have chosen the set of stellar parameters from GML1 because it is current state-of-the-art, sufficiently time-resolved, and we wanted to directly compare our 2D simulations to their 1D calculations.

Nevertheless, deviations of the stellar parameters from this set will certainly influence the results of the model calculations. Returning to the scaling laws discussed by Yorke et

al. (1982) and scaling the hydrogen-ionizing photon luminosity by \tilde{l} but keeping density and temperature constant, we find that lengths and times scale according to $\tilde{\lambda} \propto \tilde{\tau} \propto \tilde{l}^{1/3}$, velocities remain unchanged, rates of energy changes scale like $\tilde{l}^{2/3}$, and values for energy injected into the ISM at a given time like \tilde{l} . In a similar manner, a higher stellar wind luminosity will increase the size of the SWB and the energy transferred to the shell at a given time. Note that although the analytical description of the SWB evolution depends on the stellar wind luminosity, i.e. only on the product of mass-loss rate and wind terminal velocity squared, this does not account for cooling in the hot bubble which will be enhanced when the mass-loss rate rises without a proportional increase in wind velocity.

The impact of changes in the temporal evolution of the stellar parameters (e.g. a different number of outbursts of varying length) on the results of our calculations are difficult to estimate. Highly non-linear effects appear when e.g. a slow shell is overtaken by a fast wind and instabilities arise. Interaction processes between the SWB and the H II region may also be amplified or damped by variations of the stellar parameters. Numerical simulations for different stellar evolutionary histories are necessary to study these effects in detail.

Some physical processes are not yet considered in our models and we want to briefly discuss their possible influence here. One of these processes is heat conduction which may play a role for the energy transfer in the system. Though classical theory as well as our numerical models without heat conduction predict that the cooling time for the interior of the MS bubble is longer than the lifetime of the star, there is indirect evidence that, at least in NGC6888, the MS bubble is cold at the time when the WR wind blows out into the MS bubble (Mac Low 2000). A possible explanation is mass loading of the MS bubble: Heat conduction evaporates cold material from the shell or from immersed clouds which enhances the density in the bubble. The higher density reduces the cooling time of the bubble. Such evaporation from a cloud embedded in hot interstellar gas has recently been observed (Chu 2000). We will discuss the case of NGC6888 in a forthcoming paper that describes numerical simulations of the circumstellar medium around a $35 M_{\odot}$ star, a model which is more appropriate for NGC6888.

On the other hand, magnetic fields provide an efficient mechanism to reduce the efficiency of heat conduction. In a plasma the electrons are constrained to move along magnetic field lines. If the magnetic field lines are aligned with the shell or if they are tangled, the effective path lengths for fast electrons moving from the hot to the cold gas are much longer and heat conduction by electrons is less efficient. Saturation effects of heat conduction due to electric fields arising from charge separation further complicates the situation. All these effects are worthy to be studied in detail, but the simultaneous inclusion into multidimensional hydrodynamical simulations remains a computational challenge for the future.

We only allowed for isotropic winds in our models. However, line-driving theory for rotating stars suggests that mass outflow from the poles should be both more vigorous and faster. As already mentioned in section 2.4, Brighenti & D’Ercole (1997) and Frank et al. (1998) showed that anisotropic winds can indeed influence the formation and appearance of circumstellar shells, producing lobes or bipolar outflows. Similar effects may be expected for our models when anisotropic winds are employed, but details remain to be explored.

Other physical effects not yet considered in our models include variations of the metallicity in the circumstellar gas and the photodissociation of molecular hydrogen. In its later stages, the star is expected to eject gas that is enriched with metals. This enhancement of the metallicity in the circumstellar medium leads to stronger cooling and thus influences the circumstellar evolution. The dissociation of molecular hydrogen by stellar photons with energies below the Lyman threshold adds additional (exterior) layers to the basic structure shown in Figure 1. The H II region evolves into the photodissociated region which itself expands into the molecular gas. Interaction processes between the photodissociated region and the H II region similar to those between the H II region and the SWB may arise.

Finally, large scale density gradients such as those encountered at the edge of the clouds will give rise to a variety of additional dynamical effects, e.g. champagne flows of H II regions and break-out of hot gas as well as the interactions between these two phenomena.

5. Summary and conclusions

Our numerical models for the evolution of circumstellar gas around a $60 M_{\odot}$ star show that the interaction of the stellar wind bubble with the stellar radiation field can strongly influence the morphology of the circumstellar medium. The rearrangement of circumstellar gas by the stellar wind influences the way it reacts to the ionizing radiation. Density clumps formed in the shell of gas swept up by the stellar wind bubble cast shadows into the H II region. The resulting pressure gradients force material into the shadowed regions enhancing their density and forming neutral “spokes”, which subsequently raise the mass of the clumps in the shell. The H II region is extended in directions free of clumps. Thus, the formation of these elongated H II region “fingers” in our model occurs not only due to the ionization front instability described by García-Segura & Franco (1996), but is triggered and amplified by the redistribution of mass by the action of the stellar wind shell.

These results also shed light on the open question whether the complex structures that can be found in H II regions are primordial, i.e. relics from the time before the gas became ionized, or formed by dynamical processes in the course of the H II region evolution. While

there are strong observational indications that the former plays an important role, our results give support to the idea that the latter cannot be completely excluded: Intense structure formation in H II regions with strong stellar winds can occur even if the neutral ambient medium was initially homogeneous.

Nevertheless, these structures are only a temporary phenomenon because the extended H II region is eventually swept up by the stellar wind shell. If we compare our results at $t = 3.30$ Myr with the 1D solution of GML1, we see that, from a morphological point of view, there is basically little difference in the overall structure except for the appearance of an H II region at the inner part of the remnant shell and a few filaments in the hot bubble. Thus, the approach of GML1 to use the 1D solution for the estimation of the initial conditions for closer studies of the LBV and subsequent WR stage appears to be valid.

The structure formation induced by the interaction of the stellar radiation field with the SWB also has implications for the energy balance of the circumstellar gas, mostly via the effect that denser gas has a shorter recombination time and a higher cooling efficiency. This can be seen in the decrease of ionization and thermal energy of warm photoionized gas in the circumstellar medium during the time when the structure formation occurs in the first few 10^5 yr. Furthermore, the ionization energy lags behind the corresponding value in the model without wind by 0.1 – 0.4 dex and the thermal energy of warm gas by 0.2 – 0.6 dex for almost the entire lifetime of the star. This also implies that the H II regions around stars with winds can have a higher emission measure than undisturbed ones.

The ionization energy and the thermal energy of warm gas in the circumstellar medium are lower compared to the models without wind. Though the total mechanical wind energy is negligible compared to the accumulated energy of the Lyman continuum photons, the simulation with a stellar wind results in a kinetic energy in the circumstellar medium which is 4 times higher than in the model without wind. The total thermal energy is almost twice as high (or, subtracting the initial thermal energy of the background gas, the thermal energy that is added to the system is enhanced by a factor of 2.4). The energy transfer efficiency of the stellar Lyman continuum radiation over long time scales is so low because this radiative energy is mostly used to maintain the photoionization of hydrogen; it is lost from the system when the hydrogen recombines into levels above the ground state. By contrast, most of the energy of the stellar wind is converted into thermal energy of hot gas that accelerates the shell. The kinetic energy can be accumulated in the system for a long time unless it is dissipated, and the thermal energy of hot gas can also be saved if the density in the bubble is sufficiently low. For a plasma of solar chemical composition with $T = 10^7$ K and $n = 10^{-2} \text{ cm}^{-3}$, the cooling time in collisional ionization equilibrium is several 10^7 yr. Although the LBV phase of the star induces very rapid changes in the energy balance of the

circumstellar medium, its impact over longer time scales is limited due to the brevity of the LBV eruption.

The above conclusions regarding the inefficiency of converting the energy flux of photoionizing UV photons into kinetic energy are modified in the presence of large-scale density gradients (i.e. at the edge of a molecular cloud). Generally speaking, the resulting “champagne flow” can lead to an efficiency of about 1% for converting the stellar UV flux into kinetic energy of expansion (see Yorke 1986). The exact value for efficiency depends on the details of the problem, however; it is conceivable in some cases that the champagne phase is negligibly short compared to the lifetime of the star. We note that simulations which assess the role of stellar winds in the presence of champagne flows are currently rare. Comerón (1997) examined the evolution of wind-driven H II regions across a density discontinuity for various parameters but without the consideration of energy transfer efficiencies.

For the simulations of HII region evolution without a stellar wind the analytical prediction for the kinetic energy in the system at the end of the star’s lifetime differs from our numerical result by less than 30 %. The analytical solution for the energy transfer efficiency in the case of the combined H II region / SWB is just an upper limit and overestimates the transfer efficiencies into kinetic energy and thermal energy by factors of 6.7 and 9.7, respectively.

This detailed examination is suitable to improve studies of the energization of the ISM in the solar neighborhood (e.g. Abbott 1982), which use energy transfer efficiencies as theoretical input. It is also important when considering the heating of the galactic disk as a global phenomenon self-regulated by star formation. To address this the effects of overlapping H II regions and SWBs in OB clusters and associations still need to be assessed, the subject of a future investigation.

We thank Sabine Richling, Don Cox, Mordecai-Mark Mac Low, José Franco, Ralf-Jürgen Dettmar, and Matthias Wrigge for helpful comments and interesting discussions. This work was supported by the Deutsche Forschungsgemeinschaft (DFG) under grant number He 1487/17, by the Graduiertenkolleg GRK 118 in Bochum, and by the National Aeronautics and Space Administration (NASA) under grant NRA-99-01-ATP-065. Part of the research described in this paper was conducted at the Jet Propulsion Laboratory (JPL), California Institute of Technology. TF also gratefully acknowledges financial support by the German Academic Exchange Service (Doktorandenstipendium HSP II / AUFE) and the hospitality of the Department of Physics at the University of Wisconsin–Madison during a research visit. The computations were performed at the Rechenzentrum der Universität Kiel, the Konrad-Zuse-Zentrum für Informationstechnik in Berlin, and the John von Neumann-Institut für

Computing in Jülich. We also wish to thank an anonymous referee for valuable comments.

REFERENCES

- Abbott, D. C. 1982, ApJ, 263, 723
- Allen, C. W. 1973, *Astrophysical Quantities* (3d ed.; London: Athlone)
- Allen, D. A., & Burton, M. G. 1993, Nature, 363, 54
- Arthur, S. J., Henney, W. J., & Dyson, J. E. 1996, A&A, 313, 897
- Avedisova, V. S. 1972, Soviet Astronomy, 15, 708
- Beltrametti, M., Tenorio-Tagle, G., & Yorke, H. W. 1982, A&A, 112, 1
- Benaglia, P., & Cappa, C. E. 1999, A&A, 346, 979
- Bochkarev, N. G. 1988, Nature, 332, 518
- Brighenti, F., & D'Ercole, A. 1997, MNRAS, 285, 387
- Cantó, J., Raga, A., Steffen, W., & Shapiro, P. R. 1998, ApJ, 502, 695
- Cappa, C. E., & Benaglia, P. 1998, AJ, 116, 1906
- Cappa, C. E., Niemela, V. S., Herbstmeier, U., & Koribalski, B. 1996, A&A, 312, 283
- Capriotti, E. R. 1973, ApJ, 179, 495
- Castor, J., McCray, R., & Weaver, R. 1975, ApJ, 200, L107
- Chu, Y.-H. 1982, ApJ, 254, 578
- Chu, Y.-H. 2000, in Rev. Mexicana Astron. Astrofis. Ser. de Conf. 9, *Astrophysical Plasmas: Codes, Models, and Observations*, ed. J. Arthur, N. Brickhouse, & J. Franco (Mexico, DF: Inst. Astron., UNAM), 262
- Comerón, F. 1997, A&A, 326, 1195
- Downes, D., Genzel, R., Becklin, E. E., & Wynn-Williams, C. G. 1981, ApJ, 244, 869
- Dyson, J. E. 1973, A&A, 23, 381
- Dyson, J. E., & de Vries, J. 1972, A&A, 20, 223

- Falle, S. A. E. G. 1975, A&A, 43, 323
- Frank, A., Ryu, D., & Davidson, K. 1998, ApJ, 500, 291
- García-Segura, G., & Franco, J. 1996, ApJ, 469, 171
- García-Segura, G., & Mac Low, M.-M. 1995, ApJ, 455, 145
- García-Segura, G., Mac Low, M.-M., & Langer, N. 1996a, A&A, 305, 229 (GML1)
- García-Segura, G., Langer, N., & Mac Low, M.-M. 1996b, A&A, 316, 133
- Genzel, R., & Stutzki, J. 1989, ARA&A, 27, 41
- Hester, J. J., et al. 1996, AJ, 111, 2349
- Humphreys, R. M. 1991, in IAU Symp. 143, Wolf-Rayet Stars and Interrelations with Other Massive Stars in Galaxies, ed. K. A. van der Hucht, & B. Hidayat (Dordrecht: Kluwer), 485
- Koo, B.-C., & McKee, C. F. 1992a, ApJ, 388, 93
- Koo, B.-C., & McKee, C. F. 1992b, ApJ, 388, 103
- Lasker, B. M. 1967, ApJ, 149, 23
- Levenson, N. A., et al. 2000, ApJ, 533, L53
- Lozinskaya, T. A. 1982, Ap&SS, 87, 313
- Mac Low, M.-M. 2000, in Rev. Mexicana Astron. Astrofis. Ser. de Conf. 9, Astrophysical Plasmas: Codes, Models, and Observations, ed. J. Arthur, N. Brickhouse, & J. Franco (Mexico, DF: Inst. Astron., UNAM), 273
- Mac Low, M.-M., & Norman, M. L. 1993, ApJ, 407, 207
- Marston, A. P. 1996, AJ, 112, 2828
- Marston, A. P. 1997, ApJ, 475, 188
- Martins, F., Schaerer, D., & Hillier, D. J. 2002, A&A, 382, 999
- McCaughrean, M. J., & Mac Low, M.-M. 1997, AJ, 113, 391
- McKee, C. F., Van Buren, D., & Lazareff, B. 1984, ApJ, 278, L115

- Moffat, A. F. J., Firmani, C., McLean, I. S., & Seggewiss, W. 1982, in IAU Symp. 99, Wolf-Rayet Stars: Observations, Physics, Evolution, ed. C. W. H. de Loore, & A. J. Willis (Dordrecht: Reidel), 577
- Oey, M. S., & Massey, P. 1994, ApJ, 425, 635
- Osterbrock, D. E. 1989, Astrophysics of Gaseous Nebulae and Active Galactic Nuclei (Mill Valley: University Science Books)
- Pikel'ner, S. B. 1968, Astrophysical Letters, 2, 97
- Pilbratt, G. L., Altieri, B., Blommaert, J. A. D. L., Fridlund, C. V. M., Tauber, J. A., Kessler, M. F. 1998, A&A, 333, L9
- Pittard, J. M., Dyson, J. E., & Hartquist, T. W. 2001a, A&A, 367, 1000
- Pittard, J. M., Hartquist, T. W., & Dyson, J. E. 2001b, A&A, 373, 1043
- Raymond, J. C., & Smith, B. W. 1977, ApJS, 35, 419
- Richling, S., & Yorke, H. W. 2000, ApJ, 539, 258
- Różyczka, M. 1985, A&A, 143, 59
- Różyczka, M., & Tenorio-Tagle, G. 1985a, A&A, 147, 202
- Różyczka, M., & Tenorio-Tagle, G. 1985b, A&A, 147, 209
- Ryu, D., & Vishniac, E. T. 1988, ApJ, 331, 350
- Salas, L., et al. 1999, ApJ, 511, 822
- Sarazin, C. L., & White, R. E. 1987, ApJ, 320, 32
- Scoville, N., Kleinmann, S. G., Hall, D. N. B., & Ridgway, S. T. 1983, ApJ, 275, 201
- Soker, N. 1990, AJ, 99, 1869
- Soker, N. 1998, MNRAS, 299, 562
- Spitzer, L. 1978, Physical Processes in the Interstellar Medium (New York: Wiley)
- Stone, J. M., Xu, J., & Mundy, L. G. 1995, Nature, 377, 315
- Strickland, D. K., & Stevens, I. R. 1998, MNRAS, 297, 747

- Taylor, K. N. R., Storey, J. W. V., Sandell, G., Williams, P. M., & Zealey, W. J. 1984, *Nature*, 311, 236
- Tenorio-Tagle, G., Beltrametti, M., Bodenheimer, P., & Yorke, H. W. 1982, *A&A*, 112, 104
- van Leer, B. 1977, *J. Comput. Phys.*, 23, 276
- Vishniac, E. T. 1983, *ApJ*, 274, 152
- Vishniac, E. T., & Ryu, D. 1989, *ApJ*, 337, 917
- Weaver, R., McCray, R., Castor, J., Shapiro, P., & Moore, R. 1977, *ApJ*, 218, 377; erratum, 220, 742
- Williams, R. J. R. 1999, *MNRAS*, 310, 789
- Wrigge, M. 1999, *A&A*, 343, 599
- Wrigge, M., Wendker, H. J., & Wisotzki, L. 1994, *A&A*, 286, 219
- Yang, H., Chu, Y.-H., Skillman, E. D., & Terlevich, R. 1996, *AJ*, 112, 146
- Yorke, H. W. 1986, *ARA&A*, 24, 49
- Yorke, H. W., & Kaisig, M. 1995, *Comput. Phys. Commun.*, 89, 29
- Yorke, H. W., Bodenheimer, P., Tenorio-Tagle, G., 1982, *A&A*, 108, 25
- Yorke, H. W., & Welz, A. 1996, *A&A*, 315, 555

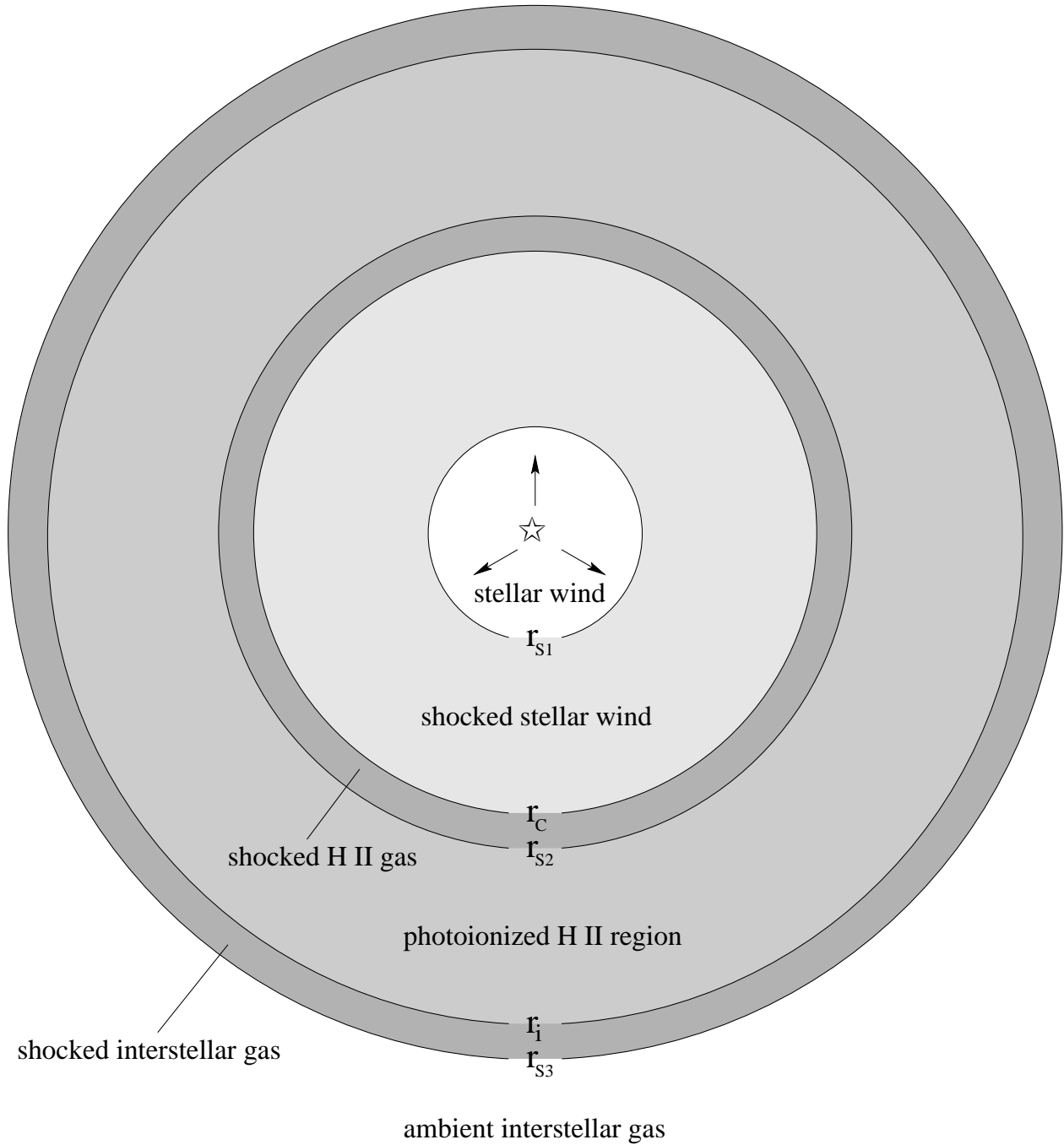


Fig. 1.— Schematic structure of an SWB: r_{s1} marks the position of the reverse shock, r_c the contact discontinuity, r_{s2} the forward shock of the stellar wind bubble, r_i the ionization front, and r_{s3} the forward shock of the H II region expansion.

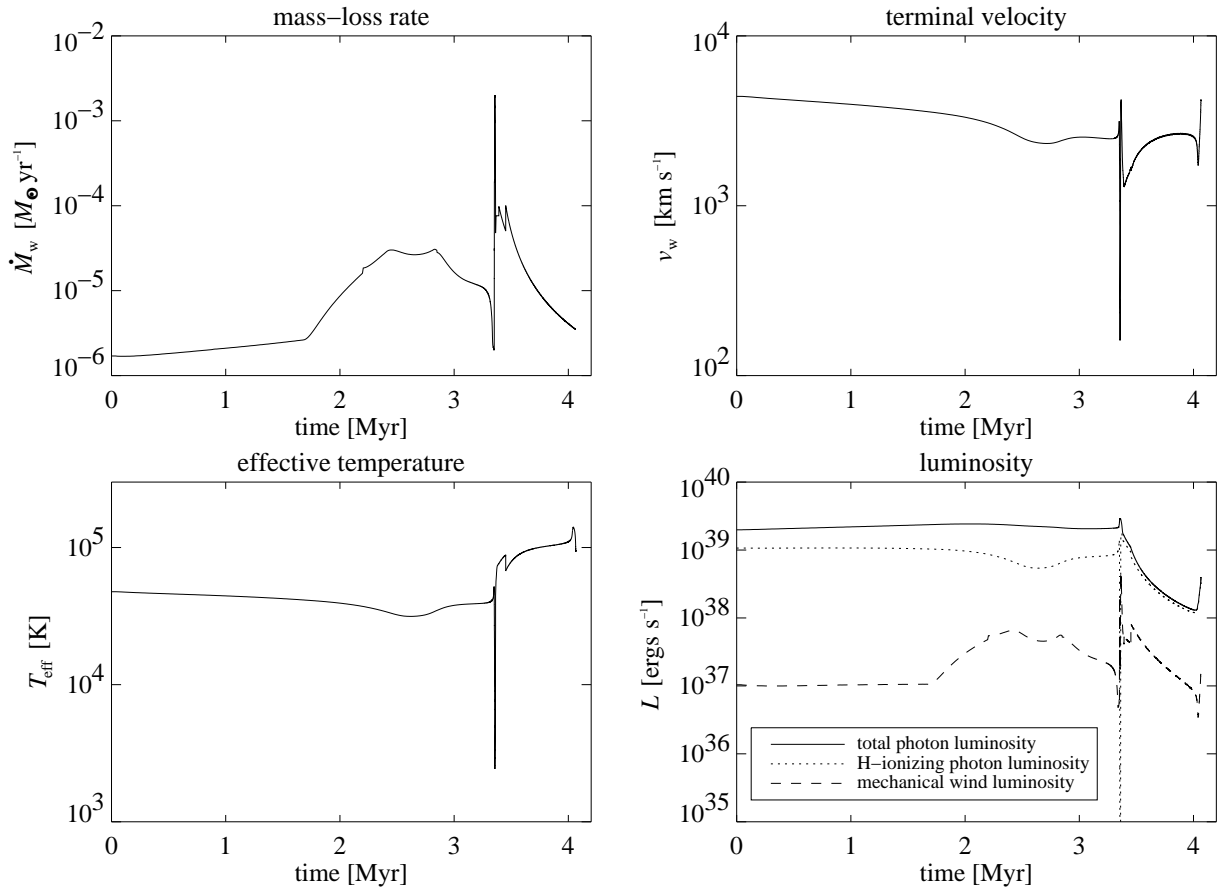


Fig. 2.— Time-dependent stellar parameters used as boundary conditions for the calculation of the $60 M_\odot$ model. Mass-loss rate (upper left diagram), terminal velocity of the wind (upper right), effective temperature (lower left), and luminosity (lower right). All parameters are adopted from GML1.

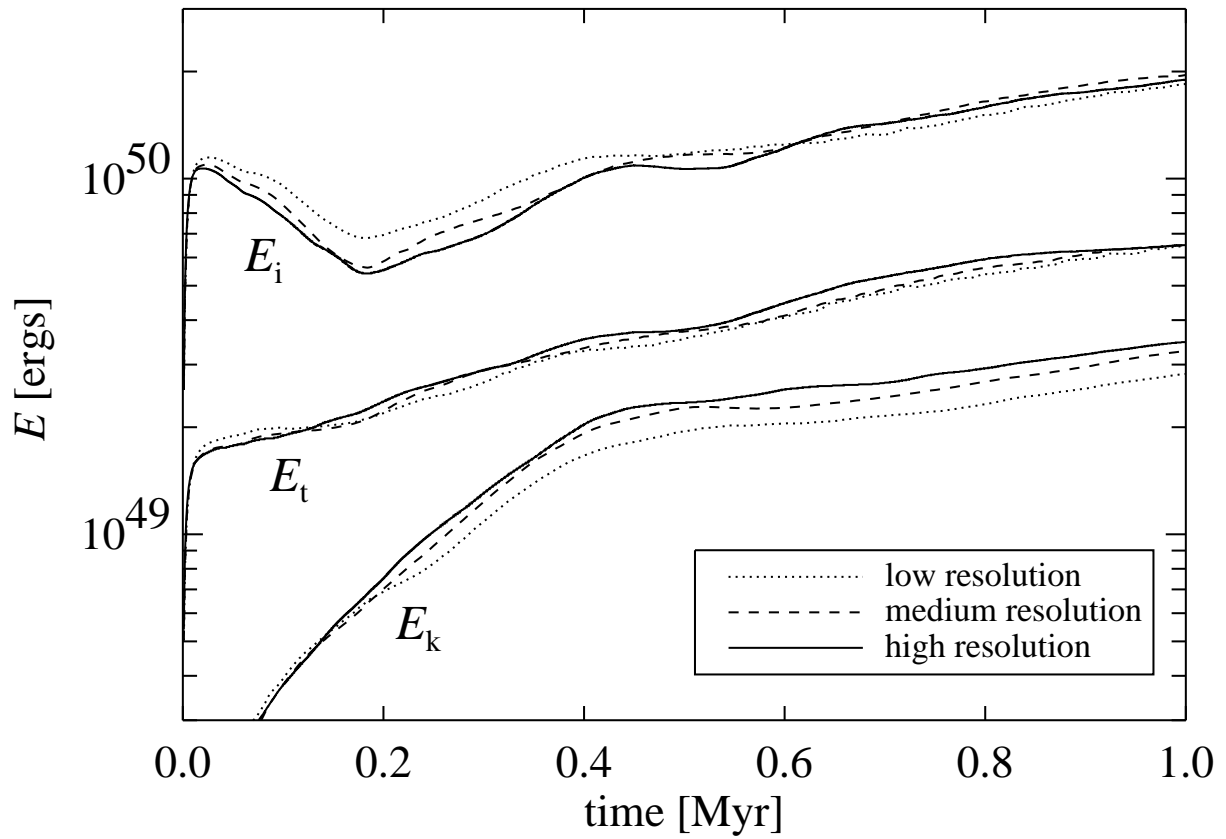


Fig. 3.— Resolution study for the $60 M_{\odot}$ model. E_k is the total kinetic energy of bulk motion in the system, E_t the thermal energy, and E_i the ionization energy (13.6 eV per ionized hydrogen atom).

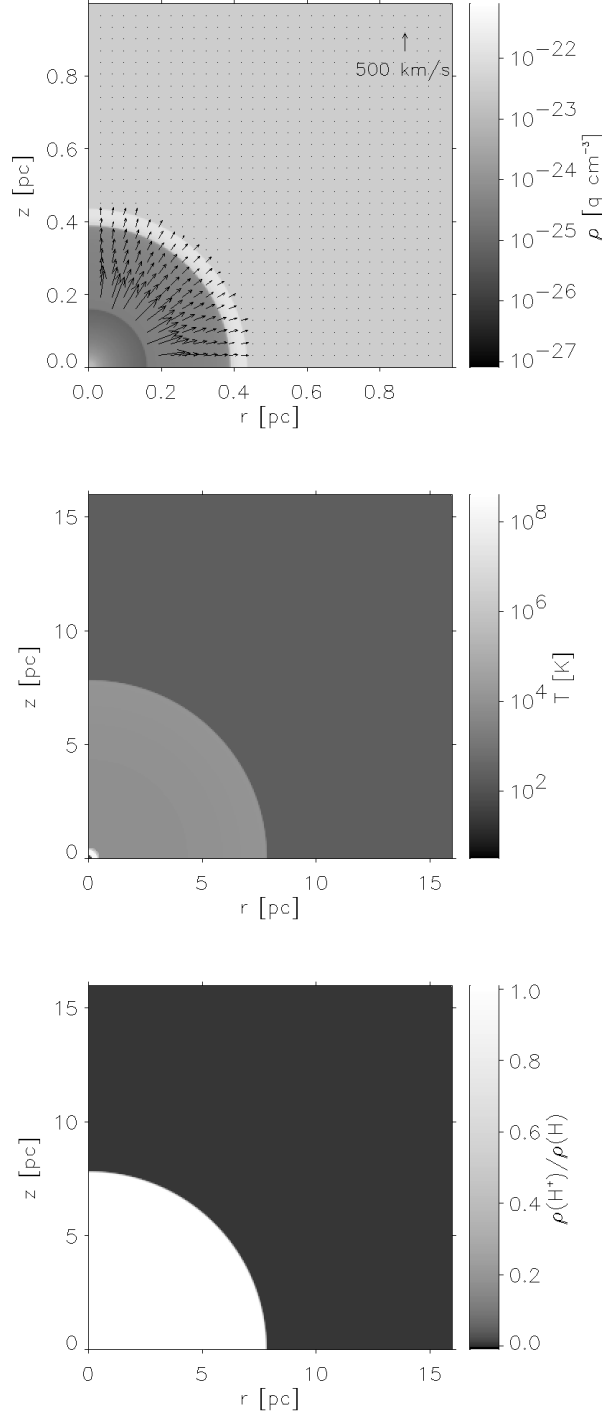


Fig. 4.— Circumstellar mass density and velocity field (top panel), temperature (center panel), and degree of hydrogen ionization (lower panel) for the $60 M_{\odot}$ model at age 10^3 yr (high resolution run). The velocity arrows in the free-flowing wind zone have been omitted to prevent confusion. The star is located in the center of the coordinate system. Please note the different length scales.

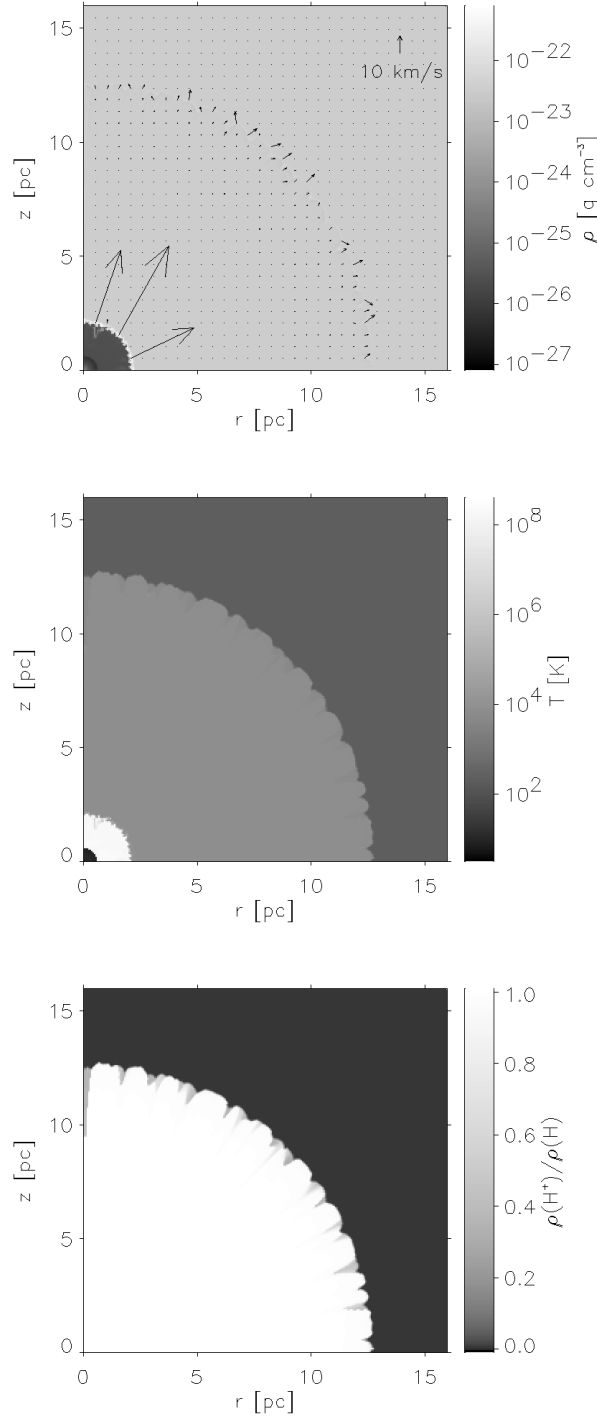


Fig. 5.— Same as Fig. 4 but at age 2×10^4 yr. The velocity arrows in the free-flowing wind zone and in the hot bubble have been omitted to prevent confusion.

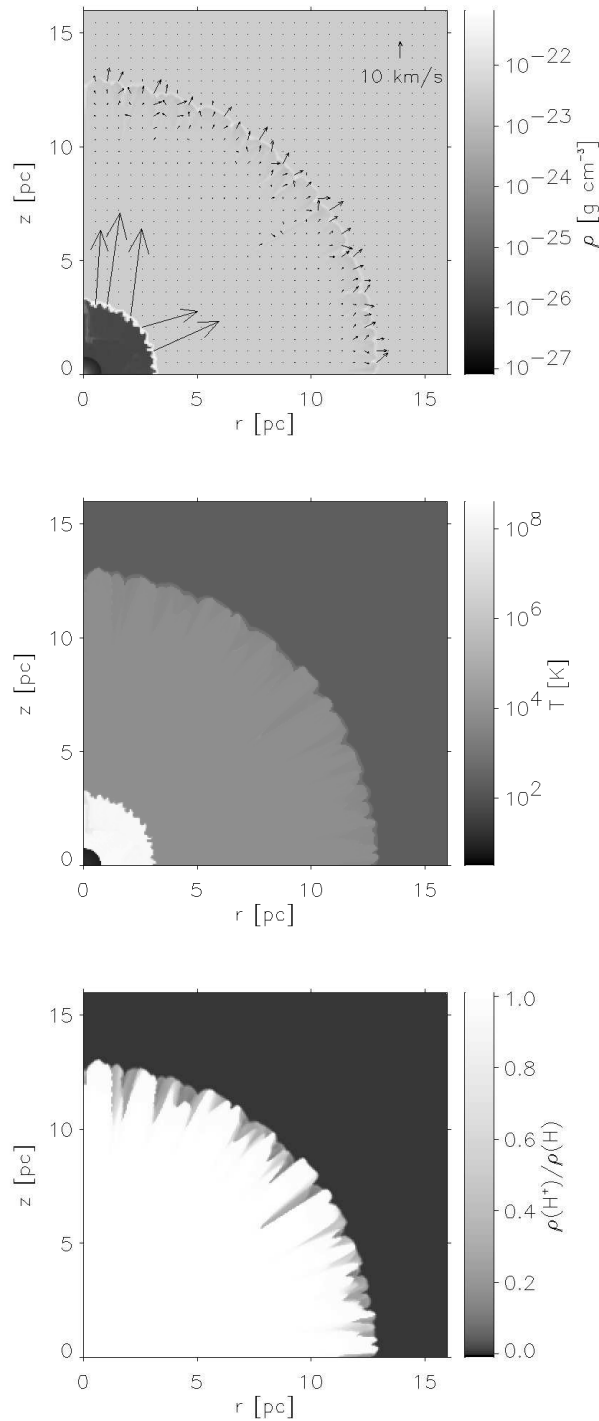


Fig. 6.— Same as Fig. 5 but at age 4×10^4 yr.

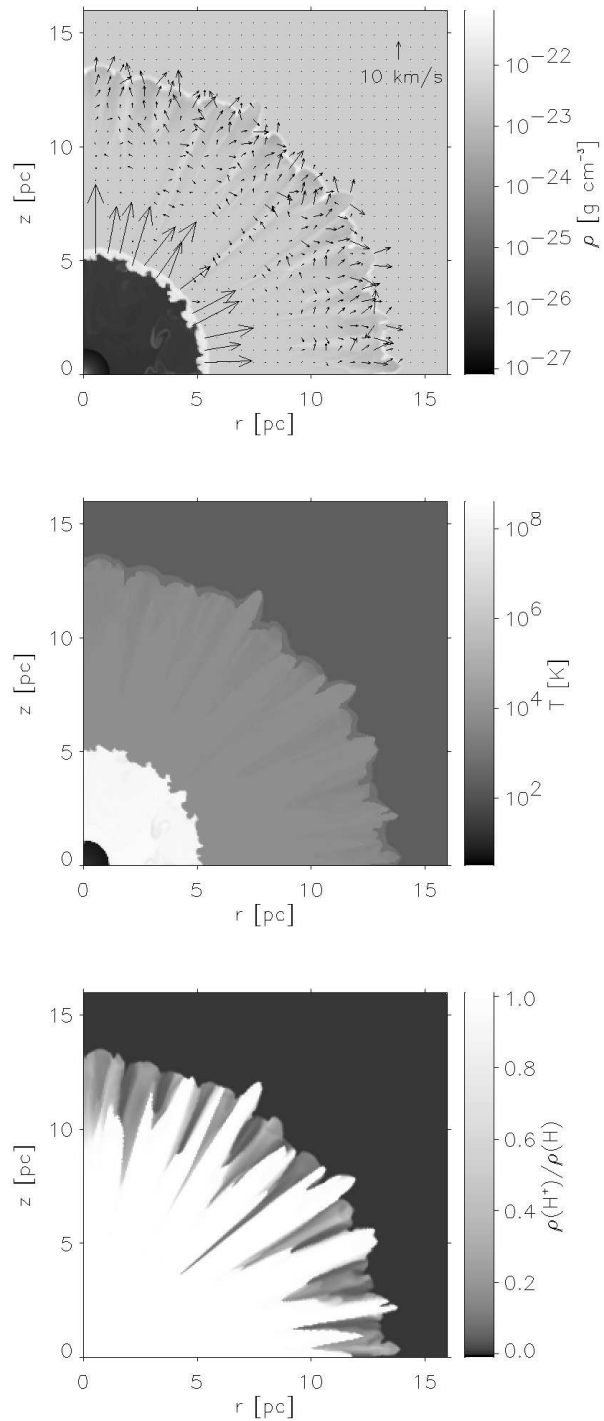


Fig. 7.— Same as Fig. 5 but at age 0.1 Myr.

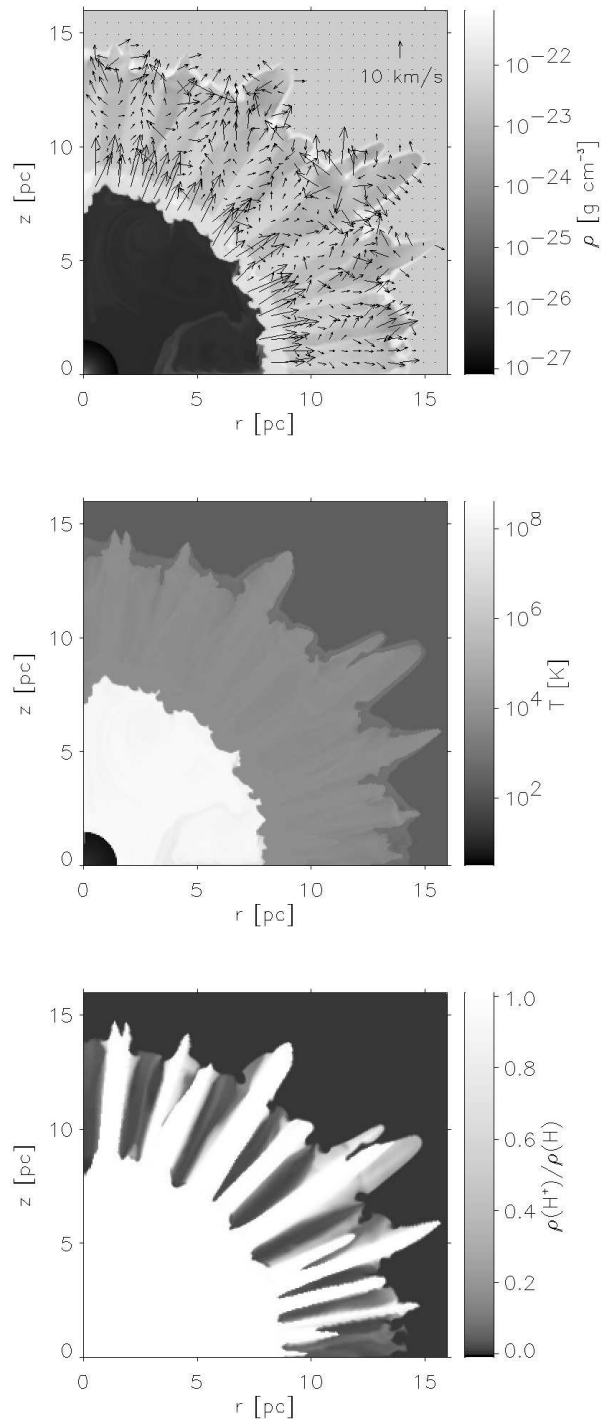


Fig. 8.— Same as Fig. 5 but at age 0.22 Myr.

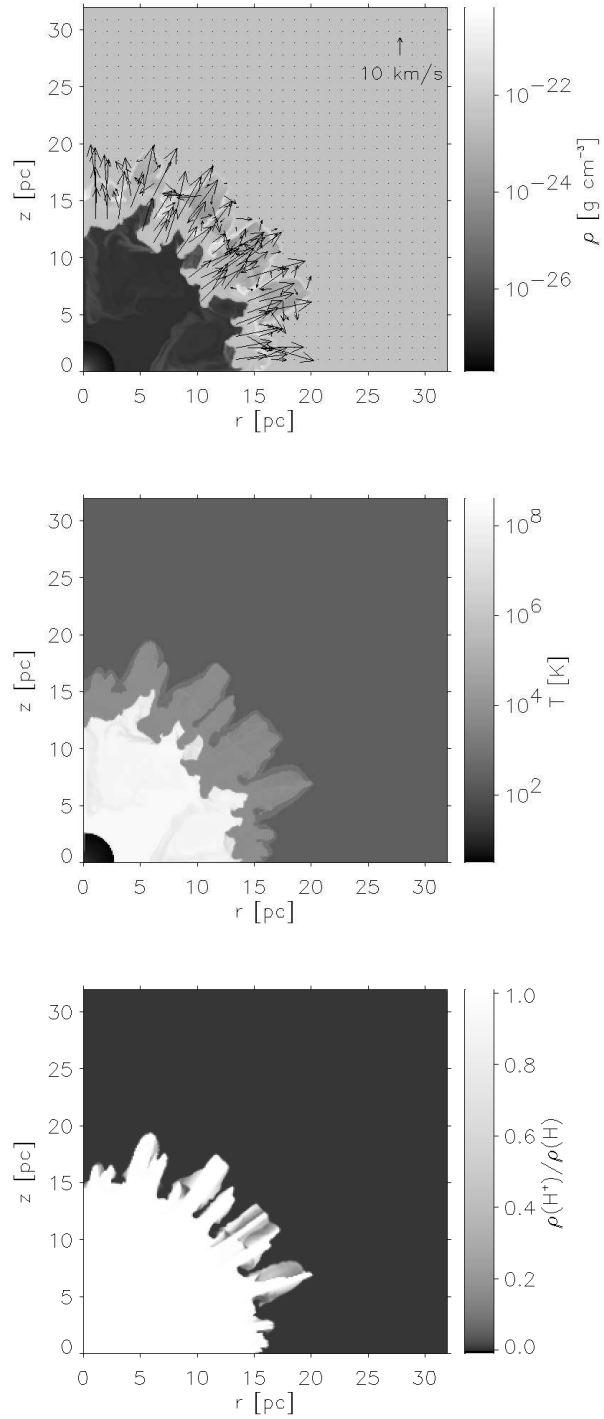


Fig. 9.— Same as Fig. 5 but at age 0.5 Myr. Because of the bubble expansion a larger volume is shown.

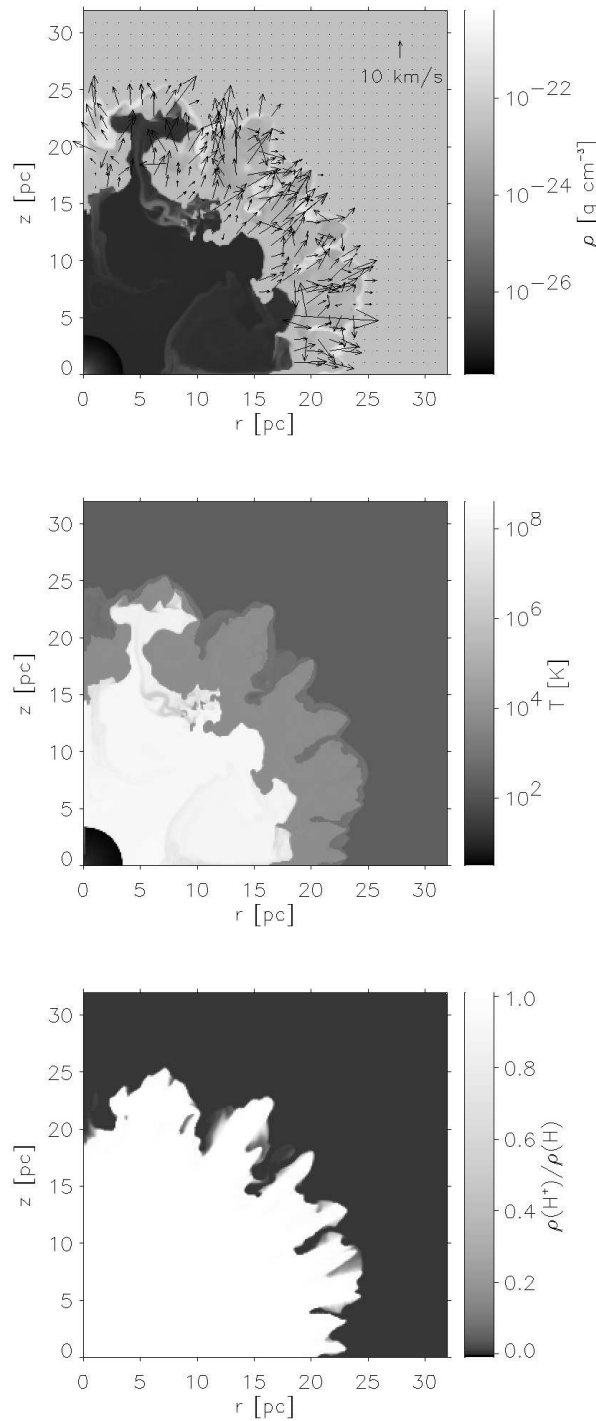


Fig. 10.— Same as Fig. 9 but at age 1 Myr.

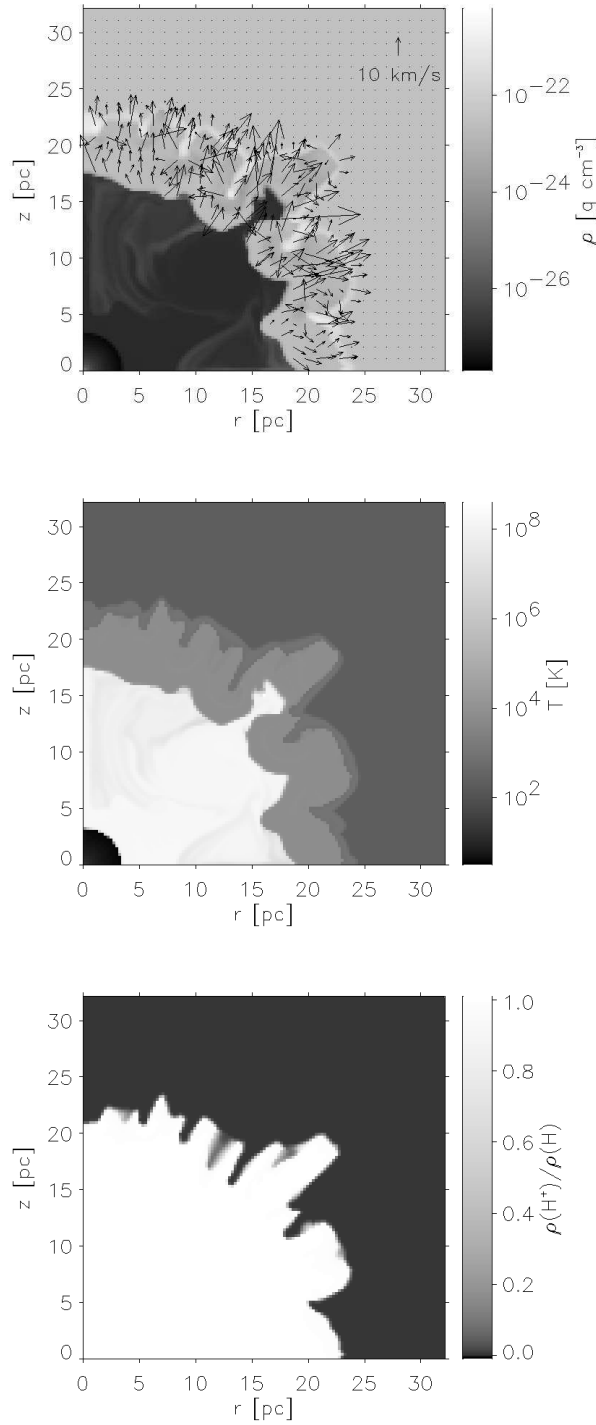


Fig. 11.— Same as Fig. 10 but for the medium resolution run.

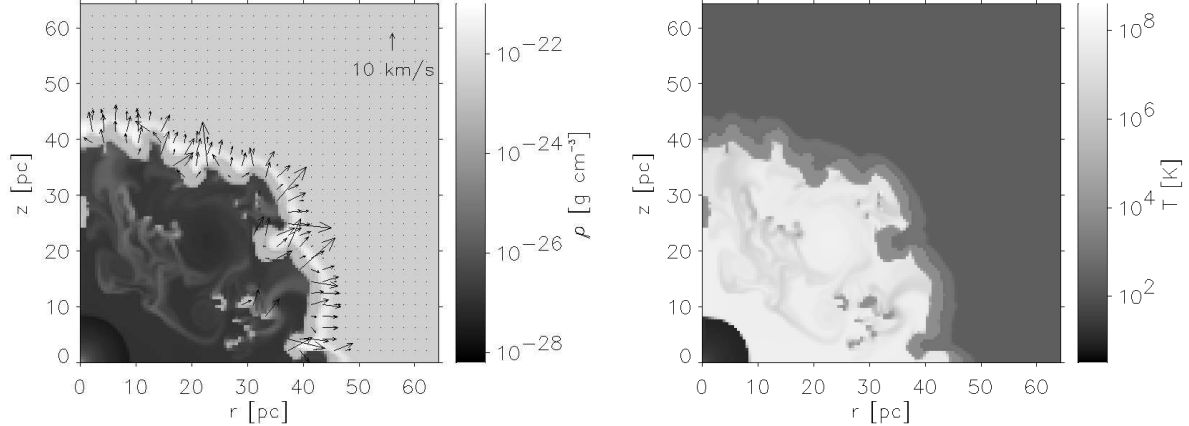


Fig. 12.— Same as Fig. 11 but at age 3.30 Myr. Only mass density and velocity field (left panel) and temperature (right panel) are shown and the displayed area is enlarged once again.

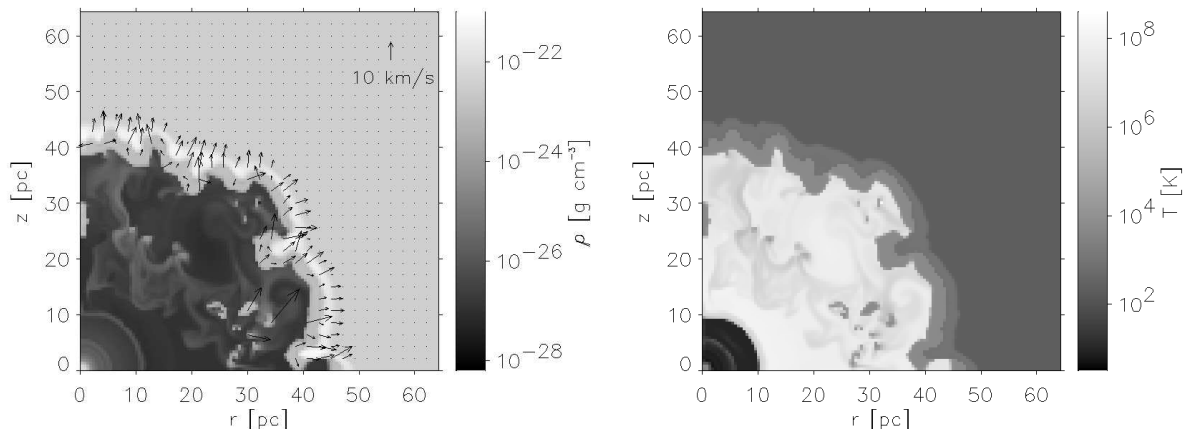


Fig. 13.— Same as Fig. 12 but at age 3.36 Myr.

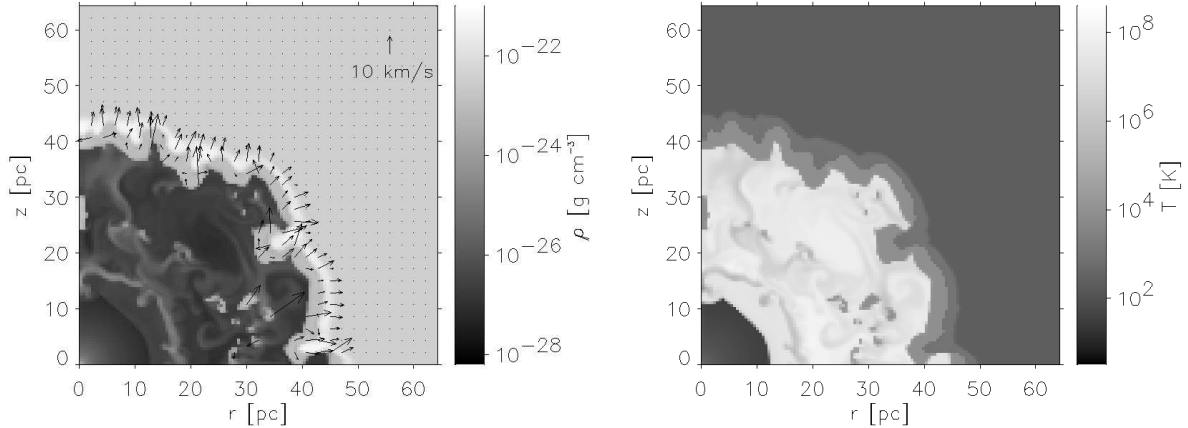


Fig. 14.— Same as Fig. 12 but at age 3.38 Myr.

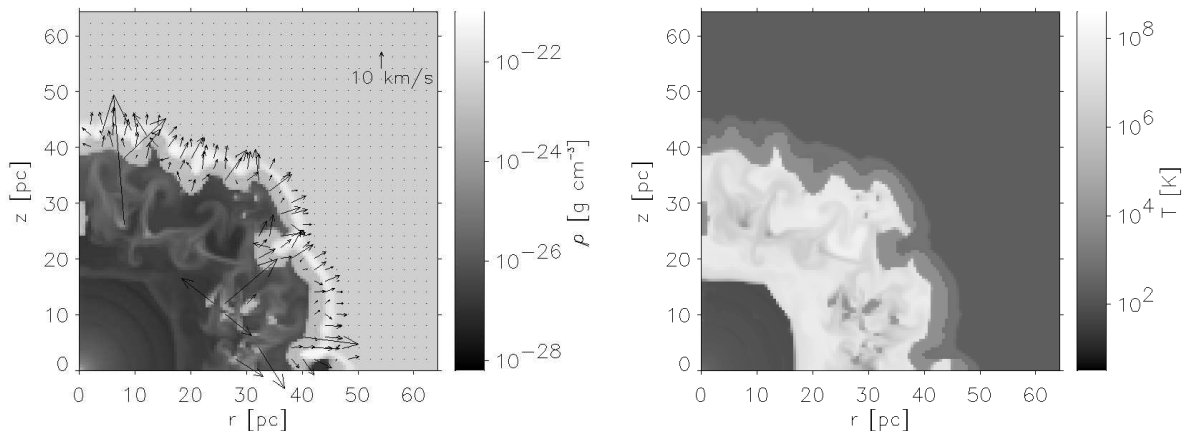


Fig. 15.— Same as Fig. 12 but at age 3.41 Myr.

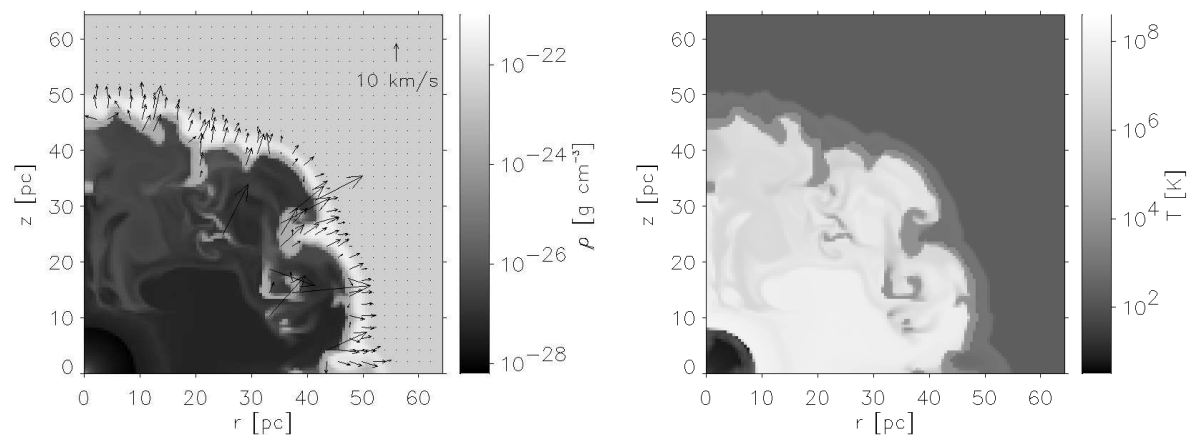


Fig. 16.— Same as Fig. 12 but at age 4.07 Myr.

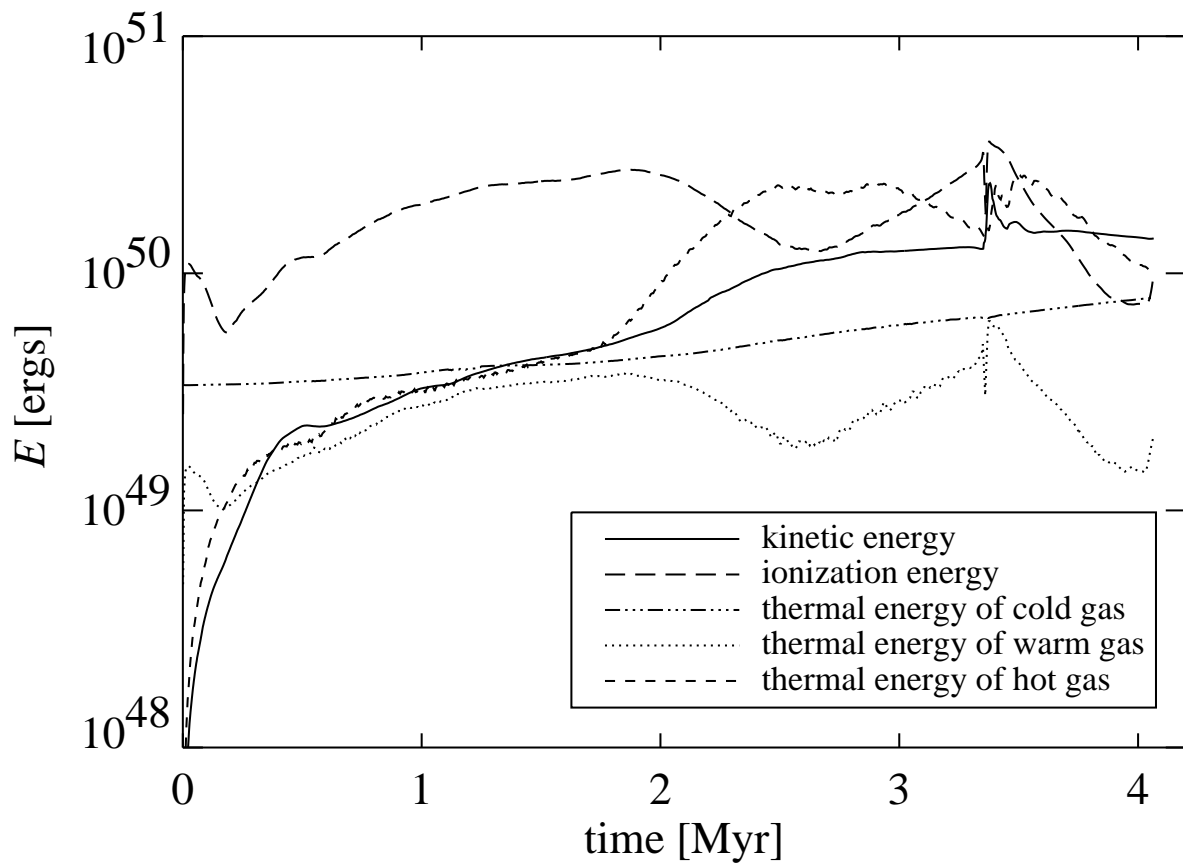


Fig. 17.— The temporal evolution of kinetic, thermal, and ionization energy in the $60 M_{\odot}$ model. For details see text.

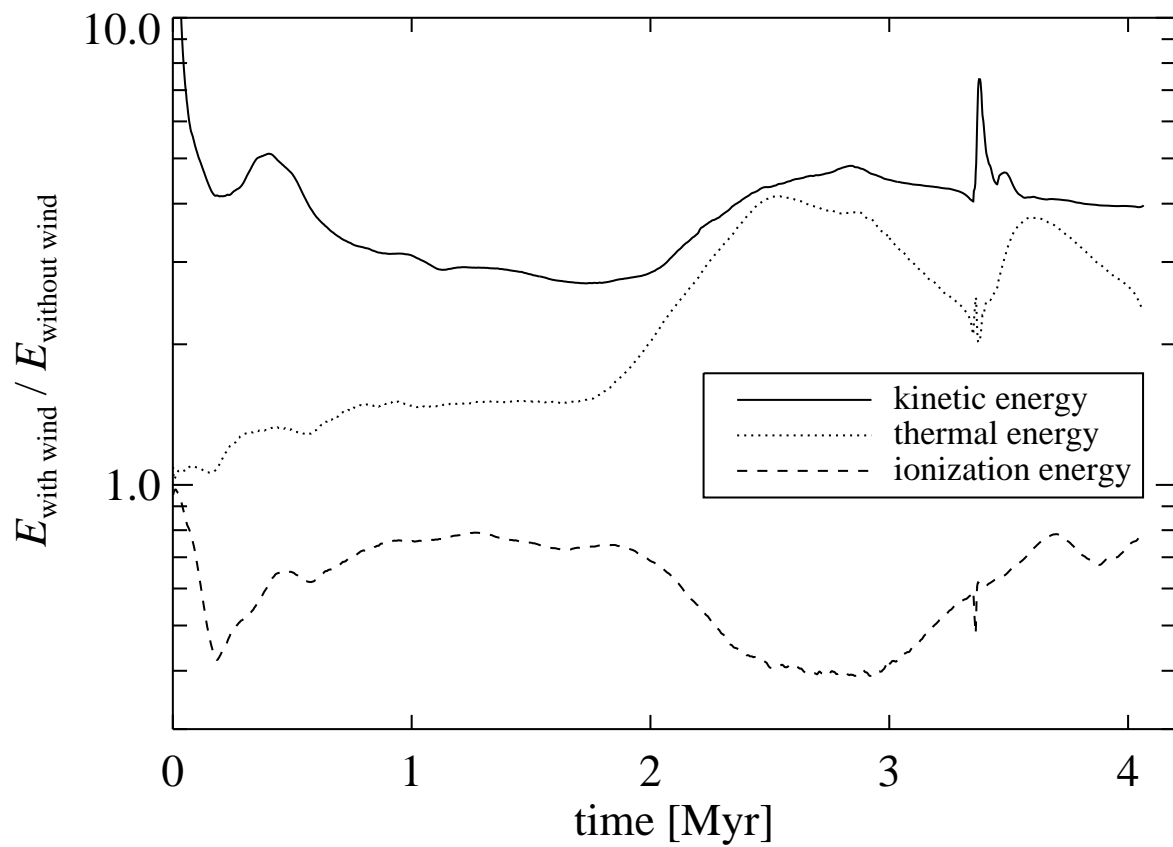


Fig. 18.— Ratio of energies in the $60 M_\odot$ model with and without a stellar wind.

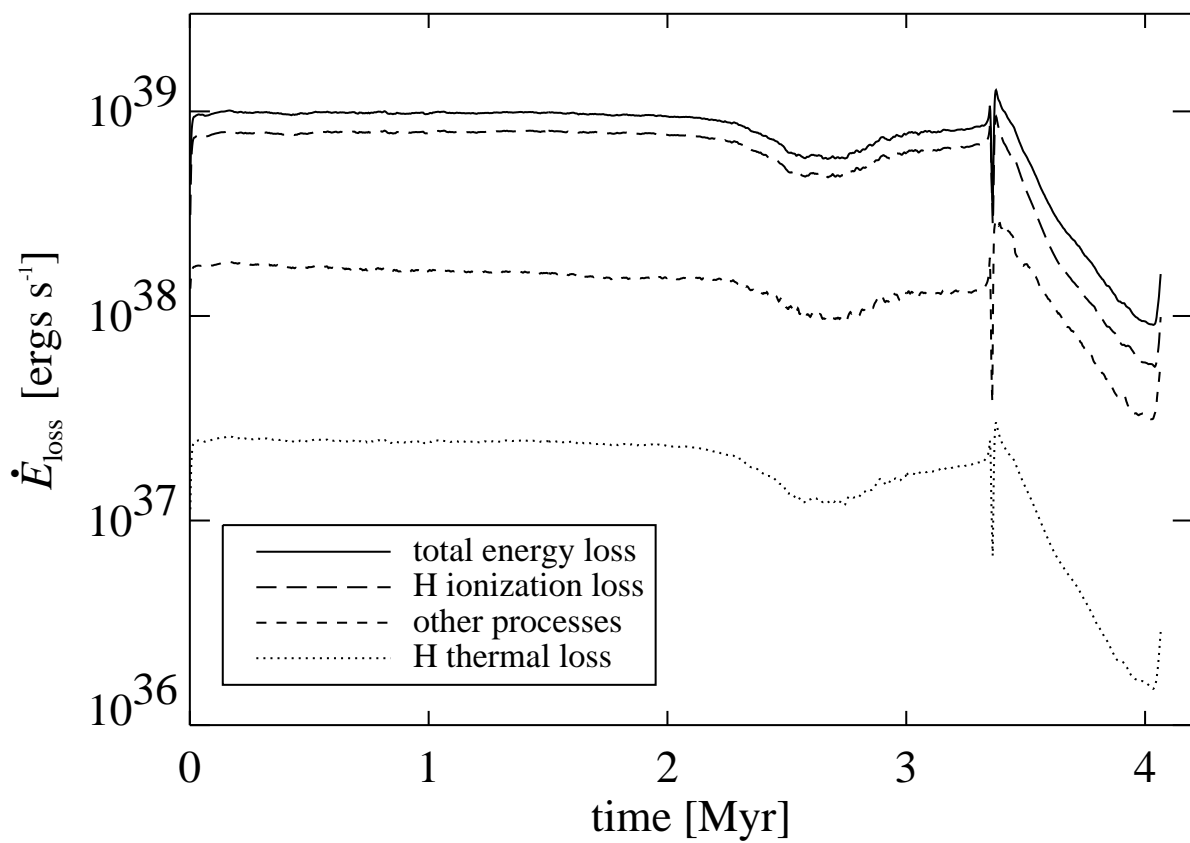


Fig. 19.— Energy loss due to cooling in the $60 M_{\odot}$ model.

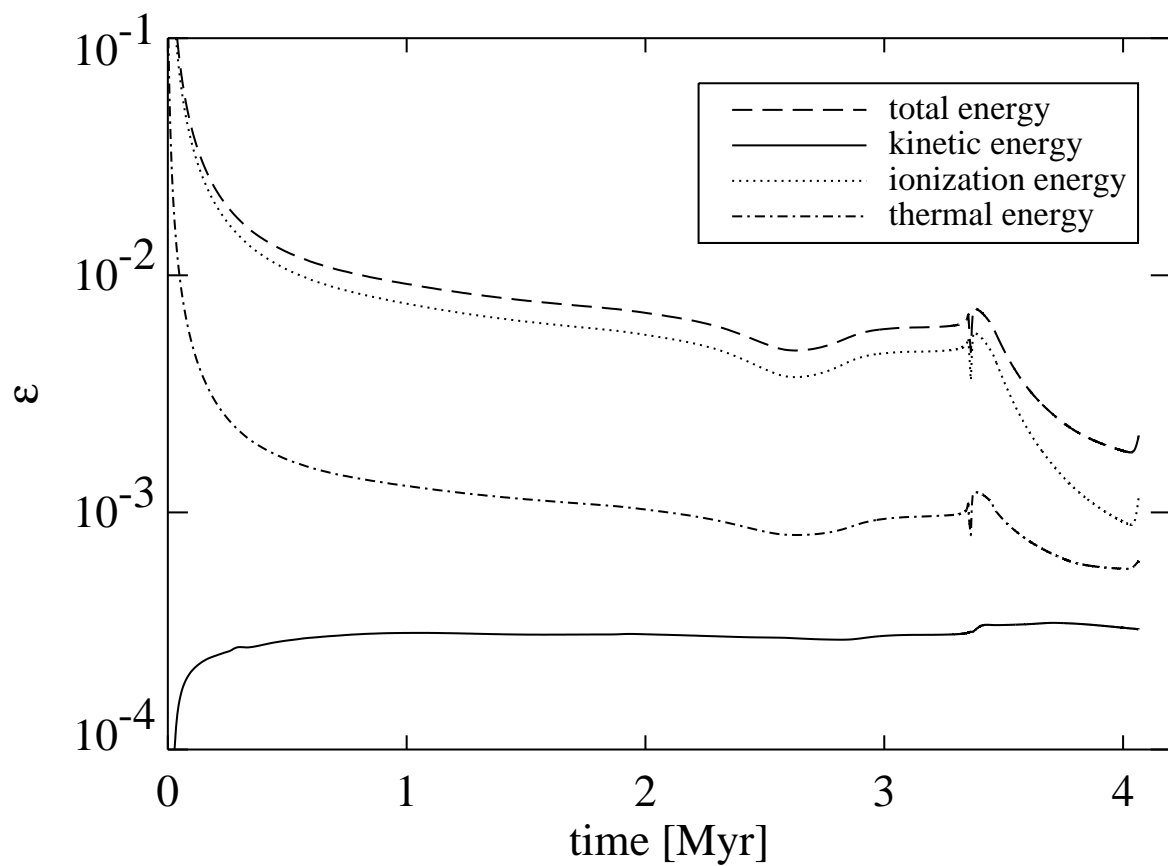


Fig. 20.— Energy transfer efficiency with respect to the total energy input in the $60 M_{\odot}$ model without wind.

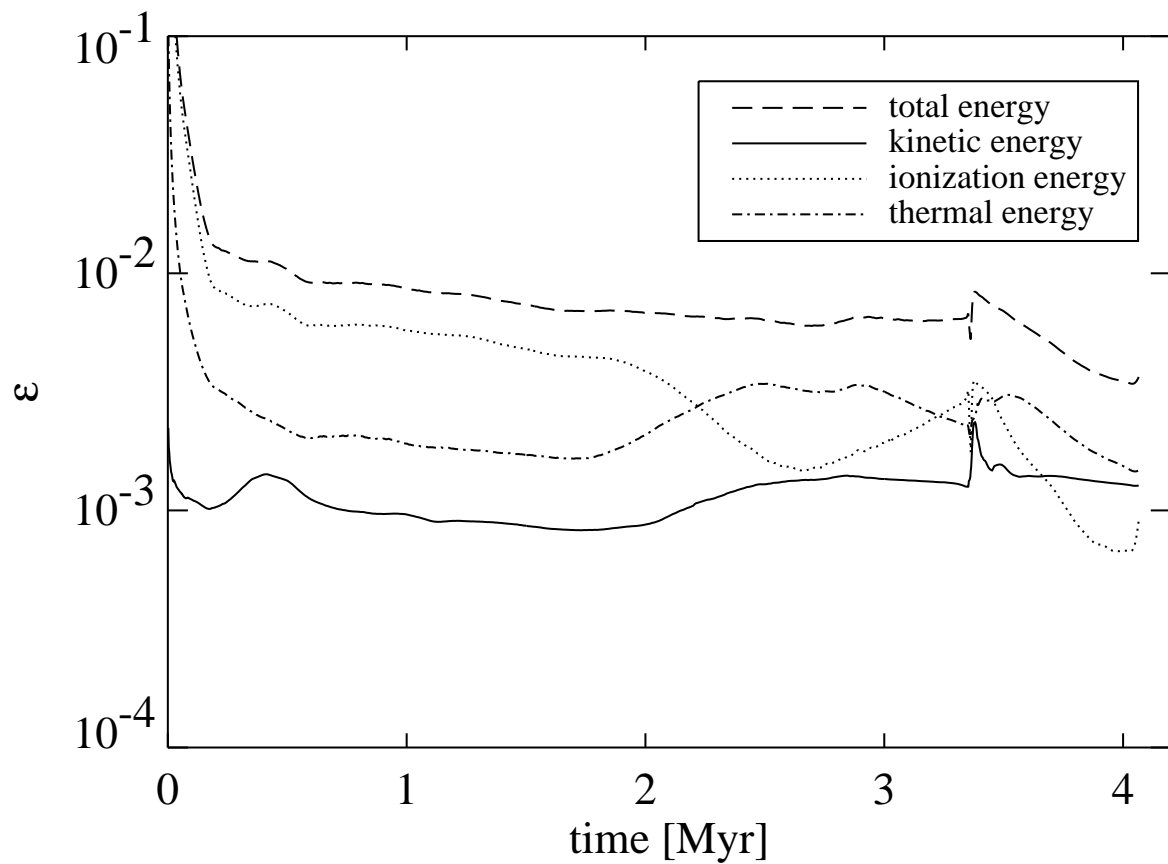


Fig. 21.— Energy transfer efficiency with respect to the total energy input in the $60 M_{\odot}$ model.

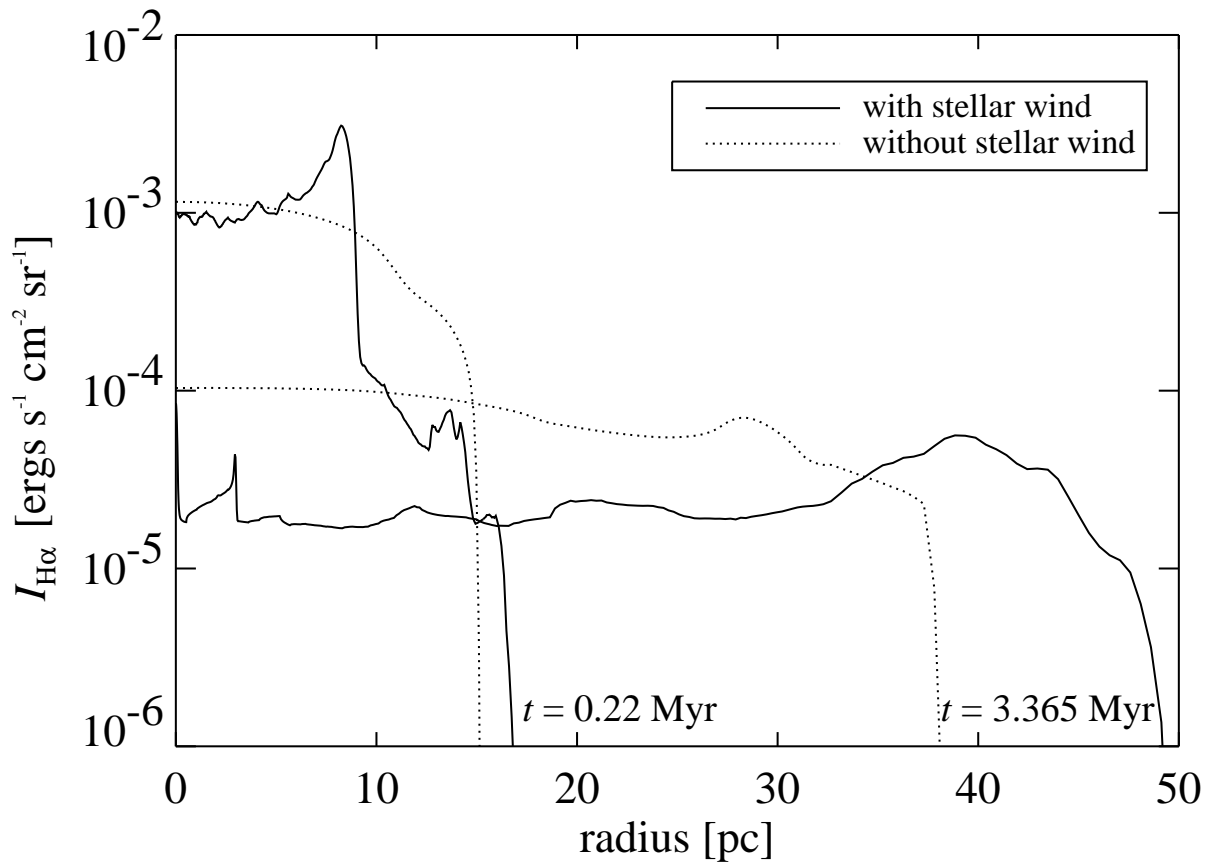


Fig. 22.— Angle-averaged H α intensity for the $60 M_\odot$ model with and without a stellar wind are compared at two evolutionary times.

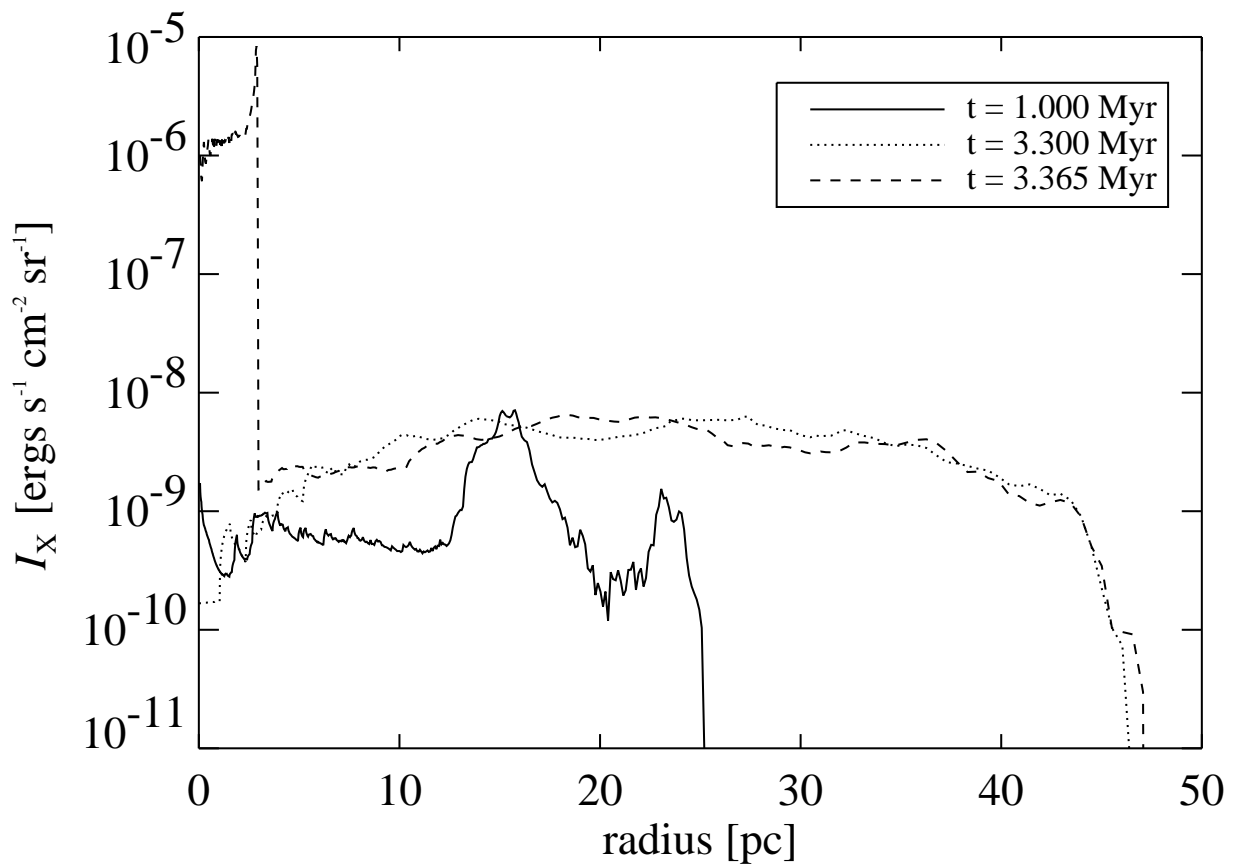


Fig. 23.— Angle-averaged soft (0.5 … 3.0 keV) X-ray intensity for the $60 M_{\odot}$ model with stellar wind at selected evolutionary times.

Table 1: Hydrodynamical models of SWBs / H II regions around single early-type stars.

Ref.	Dimensions	Geometry	Linear size (pc)	Resolution ^a (10^{-3})
1	2	cylindrical	$7.8 \dots (3.2 \times 10^{-3})$	5
2	2	spherical	0.1	5
3	1 / 2	spherical	$70 \dots 45 / 19 \dots 3$	$2.5 / 2.5 \dots 1.25$
4	2	spherical	$0.1 \dots 2$	5
5	2	spherical	$6.6 / 1$	1.3
6	2	cylindrical	0.2	3.9
7	2	cylindrical	6.5	2.5
8	2	cylindrical	64	$8.0 \dots 0.125$

Ref.	Duration (Myr)	Ionization	Heating	Cooling
1	$0.02 \dots (1.5 \times 10^{-5})$	thermal	mechanical	CIE ^b
2	10^{-3}	no	mechanical	isothermal EOS ^c
3	$4 \dots 5 / (28 \dots 7.2) \times 10^{-3}$	no	mechanical	CIE + cutoff
4	$0.02 \dots 0.33$	PIE ^d	mech. + PIE	CIE + cutoff
5	0.023	no	mechanical	CIE
6	8×10^{-4}	no	mechanical	CIE
7	0.015	no	mechanical	CIE + cutoff
8	4	time dependent ^e	mech. + radiative	explicit or CIE ^f

Ref.	Wind asymmetry	$L_w(t)$	$L_{LyC}(t)$	$n_0(r)$
1	no	fixed / two-level	0	const. / composite
2	no	two-level	0	const.
3	no	variable	variable	const. / from 1D
4	no	0	fixed	const. / power law
5	yes	two-level with trans.	0	pre WR
6	yes	three-level	0	const.
7	no	const.	0	const.
8	no	variable	variable	const.

^ain units of linear size

^bcooling function based on the assumption of collisional ionization equilibrium

^cequation of state

^dphoto ionization equilibrium calculated assuming that the gas is fully ionized inside the H II region

^ethermal and radiative ionization of hydrogen

^fexplicit calculation of important cooling processes for lower temperatures and CIE for high temperatures

References. — (1) Różyczka (1985), Różyczka & Tenorio-Tagle (1985a,b); (2) Stone et al. (1995); (3) GML1, García-Segura et al. (1996b); (4) García-Segura & Franco (1996); (5) Brighenti & D’Ercole (1997); (6) Frank et al. (1998); (7) Strickland & Stevens (1998); (8) This work.

Table 2: The energy components at the end of the simulation.

Model	E_k (10^{49} ergs)	E_i (10^{49} ergs)	$E_{t,\text{cold}}$ (10^{49} ergs)	$E_{t,\text{warm}}$ (10^{49} ergs)	$E_{t,\text{hot}}$ (10^{49} ergs)
windless	3.5	13	5.5	4.7	0
with wind	14	10	7.9	2.1	9.7

Note. — The thermal energy of the cold component, $E_{t,\text{cold}}$, contains the internal energy of the initially unperturbed ambient medium (3.4×10^{49} ergs) that has to be subtracted whenever the input of thermal energy into the system is considered.

Table 3: The energy transfer efficiencies at the end of the simulation.

Model	ε_k (10^{-4})	ε_i (10^{-4})	ε_t (10^{-4})
windless	3.3	12	6.4
with wind	13	9.1	15